NASA/TP-20260001272

Eugene Stansbery-Meter Class Autonomous Telescope Observations of the Geosynchronous Orbital Debris Environment

Observing Years: 2020-2022

Orbital Debris Program Office

B. A. Buckalew[1], C. L. Cruz[1], J. A. Headstream[2], and A. P. Manis[2]

[1]Clear Lake Group/Amentum – Amentum JETS II Contract
Houston, TX 77058

[2]National Aeronautics and Space Administration
Johnson Space Center
Houston, TX 77058

February 2026

NASA STI Program Report Series

The NASA STI Program collects, organizes, provides for archiving, and disseminates NASA's STI. The NASA STI program provides access to the NTRS Registered and its public interface, the NASA Technical Reports Server, thus providing one of the largest collections of aeronautical and space science STI in the world. Results are published in both non-NASA channels and by NASA in the NASA STI Report Series, which includes the following report types:

- TECHNICAL PUBLICATION. Reports of completed research or a major significant phase of research that present the results of NASA Programs and include extensive data or theoretical analysis. Includes compilations of significant scientific and technical data and information deemed to be of continuing reference value. NASA counterpart of peer-reviewed formal professional papers but has less stringent limitations on manuscript length and extent of graphic presentations.

- TECHNICAL MEMORANDUM. Scientific and technical findings that are preliminary or of specialized interest, e.g., quick release reports, working papers, and bibliographies that contain minimal annotation. Does not contain extensive analysis.

- CONTRACTOR REPORT. Scientific and technical findings by NASA-sponsored contractors and grantees.

- CONFERENCE PUBLICATION. Collected papers from scientific and technical conferences, symposia, seminars, or other meetings sponsored or co-sponsored by NASA.

- SPECIAL PUBLICATION. Scientific, technical, or historical information from NASA programs, projects, and missions, often concerned with subjects having substantial public interest.

- TECHNICAL TRANSLATION. English-language translations of foreign scientific and technical material pertinent to NASA's mission.

Specialized services also include organizing and publishing research results, distributing specialized research announcements and feeds, providing information desk and personal search support, and enabling data exchange services.

For more information about the NASA STI program, see the following:

- Access the NASA STI program home page at http://www.sti.nasa.gov

- Help desk contact information:

https://www.sti.nasa.gov/sti-contact-form/
and select the "General" help request type.

NASA/TP-20260001272

Eugene Stansbery-Meter Class Autonomous Telescope Observations of the Geosynchronous Orbital Debris Environment

Observing Years: 2020-2022

Orbital Debris Program Office

B. A. Buckalew[1], C. L. Cruz[1], J. A. Headstream[2], and A. P. Manis[2]

[1]Clear Lake Group/Amentum – Amentum JETS II Contract
Houston, TX 77058

[2]National Aeronautics and Space Administration
Johnson Space Center
Houston, TX 77058

National Aeronautics and
Space Administration

Johnson Space Center
Houston, Texas 77058

February 2026

ACKNOWLEDGEMENTS

Thanks to Susan Lederer, James Frith, and Paul Hickson for contributing to the past acquisition and analysis with ES-MCAT. Thanks to all our interns that helped with manual review of this GEO survey and with all other components dealing with ES-MCAT. These people include but are not limited to Jarod Melo, Kayley Green-Tooney, and Glen Beran. Thanks to Randall Alliss for his work in updating the weather downtime on Ascension Island. And thanks to all organizations and personnel involved with creating and facilitating ES-MCAT operations.

TABLE OF CONTENTS

SECTION **PAGE**

LIST OF FIGURES

LIST OF TABLES

Abbreviations/Acronyms

ACO	Assumed Circular Orbit
CCD	Charge-Coupled Device
CDT	CCD Debris Telescope
CIF	Consolidated Instrumentation Facility
CIS	Commonwealth of Independent States
CT	Correlated Target
CY	Calendar Year
Dec	Declination
DOY	Day of Year
EL	Elevation
ES-MCAT	Eugene Stansbery-Meter Class Autonomous Telescope
EVAL	Expectation Value
FCF	Field Center File
FLIR	Forward-Looking Infrared
FOV	Field of View
FWHM	Full Width at Half Maximum
FY	Fiscal Year
GEO	Geosynchronous Orbit
HA	Hour Angle
INC	Inclination
JAO	John Africano Observatory
JRBT	James R. Benbrook Telescope
JSC	Johnson Space Center
LEO	Low Earth Orbit
LMT	Liquid Mirror Telescope
LST	Local Sidereal Time
MODEST	Michigan Orbital Debris Survey Telescope
MTO	MEO-transfer Orbit
NASA	National Aeronautics and Space Administration
OCS	Observatory Control System
ODPO	Orbital Debris Program Office
OSEM	Optical Size Estimation Model
QE	Quantum Efficiency
RA	Right Ascension
RAAN	Right Ascension of the Ascending Node
RMS	Root Mean Square
ROI	Region of Interest
RSO	Resident Space Object
SNR	Signal-to-Noise Ratio
SATRAK	Satellite Trajectory and Attitude Kinetics
SGP	Simplified General Perturbations code
SSN	U.S. Space Surveillance Network
ST	Sidereal-tracked

TLE	Two-line Element Set
UCT	Uncorrelated Target
USSF	United States Space Force
UT	Universal Time
UTC	Coordinated Universal Time

(This page intentionally left blank)

1.0 Introduction

1.1 PURPOSE

This report summarizes optical measurement data of the orbital debris (OD) environment in geosynchronous orbit (GEO) from the Eugene Stansbery-Meter Class Autonomous Telescope (ES-MCAT), operated by the National Aeronautics and Space Administration (NASA) Orbital Debris Program Office (ODPO).

1.2 SCOPE

The period covered by this report includes data collected from 14 April 2020 through 12 April 2022, representing the first GEO survey completed with ES-MCAT. Results presented in this report represent a broad overview of the current state of the OD environment in GEO as measured by ES-MCAT. Unique effects from the COVID-19 global pandemic on ES-MCAT observations are also discussed.

1.3 BACKGROUND

The ODPO, located at NASA Johnson Space Center (JSC), is the lead office performing a full spectrum of orbital debris research and mission support activities. This office is the recognized world leader in conducting measurements of the debris environment and in developing the technical consensus for adopting mitigation measures to protect users of the orbital environment.

The ODPO has maintained a measurement program using remote sensing techniques such as radars and optical telescopes to measure the debris populations from low Earth orbit (LEO) to GEO. Data collected to help characterize the debris environment are critical for building and validating models such as the NASA Orbital Debris Engineering Model (ORDEM) (Manis, Matney and Vavrin, et al. 2022, Kennedy, et al. 2022). ORDEM is designed to facilitate modeling assessments by spacecraft owner/operators as well as for ground-based observation planning by providing debris fluxes in terms of debris size, orbits, and material densities (Matney, Manis, et al. 2019, Matney, Anz-Meador, et al. 2023). Information on trackable objects comes from the publicly available Space Surveillance Network (SSN) catalog, which provides data on objects down to approximately 10 cm in LEO and approximately 1 m in GEO. Below those sizes, the ODPO relies on specialized sensors capable of detecting objects at smaller size ranges to statistically sample the orbital debris environment on a regular basis and provide the data inputs for updating and validating ORDEM.

While both ground-based radar and optical sensors possess the capability to observe and characterize debris in LEO, optical sensors are predominantly used when observing small debris in deep space orbits such as elliptical geosynchronous transfer orbits (GTO), medium Earth orbit (MEO), and GEO. The ODPO has developed the John Africano Observatory (JAO) and ES-MCAT to provide dedicated optical sensors capable of observing small debris in each of these environments. NASA uses JAO to help characterize this environment in GEO in terms of magnitude (which can be converted to size using an optical size estimation model (OSEM)) and orbital information. The objectives for this survey are to determine the extent and character of

debris in GEO, specifically by obtaining distributions for the brightness, inclination (INC), right ascension of ascending node (RAAN), and mean motion for the debris.

While relative velocities of debris residing in GEO are much lower than in LEO, the GEO environment's debris population still has a high potential for collision with operational satellites due to the extremely long lifetimes of debris and satellites as well as the limited toroidal volume. Space-faring nations have been placing satellites into GEO since the mid- to late 1960s. Along with operational satellites, the population of debris in GEO – including dead satellites, rocket body upper stages, deployment hardware, fragmentation debris, *etc*. – has also grown, primarily due to accidental explosions. Prior to this survey, eight breakup events have occurred in the GEO environment (see Table 1) (Anz-Meador, Opiela and Liou 2022). The first was the 1978 breakup of the EKRAN-2 satellite, (international designator 1977-092A, SSN #10365), for which four fragments are currently cataloged. EKRAN-4 and EKRAN-9 had breakup events in 1981 and 1983, respectively. No debris pieces from those events have been cataloged to date. In 1992, a Titan 3C Transtage breakup (international designator 1968-081E, SSN #3432) produced at least 28 pieces of debris. Ground-based Electro-Optical Deep Space Surveillance (GEODSS) telescopes tracked these objects for a few days after the event; two pieces have been lost. On 16 January 2016, a Briz-M rocket body (international designator 2015-075B, SSN #41122) experienced a breakup event, and six pieces from that event are still cataloged by the SSN. The Chinese GPS satellite named Compass G2, (international designator 2009-018A, SSN #34779), had an event on 24 June 2016. The last two GEO events involved Titan 3C Transtage rocket bodies with one occurring on 28 February 2018 and one on 7 May 2019. The parent bodies were SSN#3692 (international designator 1969-013B) and SSN #8751 (international designator 1976-023F), respectively. At the time of writing, approximately 18 objects associated with SSN #3692 are being tracked.

Table 1. Confirmed GEO breakup events prior to the completion of this survey.

Satellite Name	International Designator	SSN Catalog Number	Launch Date	Breakup Date
Ekran 2	1977-092A	10365	20 Sep 1977	23 Jun 1978
Ekran 4	1979-087A	11561	3 Oct 1979	23 Apr 1981
Ekran 9	1982-093A	13554	16 Sep 1982	23 Dec 1983
Titan 3C Transtage R/B (OV2-5 R/B)	1968-081E	3432	26 Sep 1968	21 Feb 1992
Breeze-M R/B (Cosmos 2513 R/B)	2015-075B	41122	13 Dec 2015	16 Jan 2016
BeiDou G2	2009-018A	34779	14 Apr 2009	29 Jun 2016
Titan 3C Transtage R/B (OPS 0757 [TACSAT] R/B)	1969-013B	3692	9 Feb 1969	28 Feb 2018
Titan 3C Transtage R/B (LES 8,9/SOLRAD 11A,B R/B)	1976-023F	8751	15 Mar 1976	7 May 2019

In early optical surveys, NASA used the Charge-Coupled Device (CCD) Debris Telescope (CDT), a transportable 32-cm Schmidt telescope. The CDT was shipped to the Hawaiian island of Maui for a survey of the GEO environment conducted by NASA from 1992 through 1994. Results from the survey indicated that down to a limiting apparent magnitude of 17 (~60 cm in diameter), about 27% of all objects in GEO are debris. The actual debris population is expected to be much larger because debris smaller than 60 cm in diameter should exist in GEO, consistent with detections of debris in LEO. NASA moved the CDT to Cloudcroft, New Mexico, for further GEO studies where data were collected from November 1997 to December 2001. The CDT determined the right ascension and declination rates at which most GEO objects are traveling (K. J. Abercromby, P. Seitzer and H. M. Cowardin, et al. 2011). Also located at Cloudcroft, New Mexico, the 3-m Liquid Mirror Telescope (LMT) was NASA's primary research facility to optically characterize the LEO debris environment from October 1997 to December 2001.

In 2001, the ODPO transitioned to using the Michigan Orbital Debris Survey Telescope (MODEST) as its primary optical sensor for GEO. MODEST was a contributing sensor to the ODPO's measurement efforts from 2001 to 2014. For the first time, the ODPO conducted comprehensive statistical surveys of the GEO belt. During MODEST's time, three separate surveys were conducted. Those survey years were 2002-03 (K. J. Abercromby, P. Seitzer and E. S. Barker, et al. 2010); 2004-06 (K. J. Abercromby, P. Seitzer and E. S. Barker, et al. 2010); 2007-09 (K. J. Abercromby, P. Seitzer and H. M. Cowardin, et al. 2011); and 2013-14. The results of these surveys were originally used to validate GEO belt populations for ORDEM 3.0 (Stansbery, et al. 2015) as well as to build and validate GEO populations for ORDEM 3.1 (Manis, Matney and Anz-Meador, et al. 2019, Matney, Manis, et al. 2019). The methodology and results from the MODEST surveys have aided the design of surveys using ES-MCAT, which is described below.

2.0 Optical System Overview

ES-MCAT is located on Ascension Island, part of the Saint Helena British Overseas Territory, and located at 7° 58′ 20″ S, 14° 24′ 4″ W. The remote location was chosen as an ideal location for an observatory for several reasons. With no right to abode for the island, the skies are extremely dark when the moon is below the horizon ($M_V > 21$ mag/arcsecond^2). Ascension has a United States Space Force (USSF) auxiliary air base on island, so infrastructure for running an observatory was already in place. Finally, an optical observatory on Ascension would fill a gap in the GEODSS coverage as shown in Figure 1. Because of this gap in coverage, the Air Force

Research Laboratory collaborated with NASA to construct JAO on island.

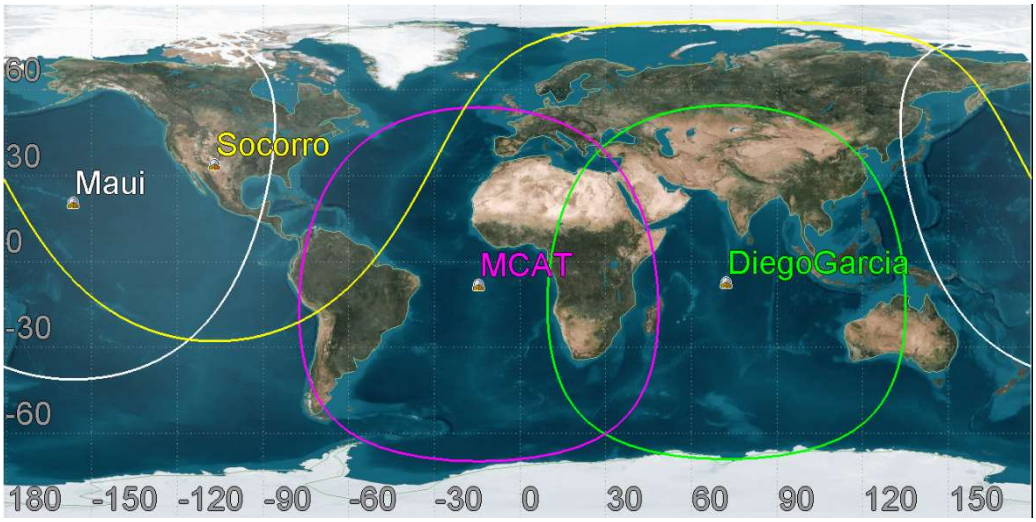

Figure 1. Map showing locations of all current dedicated GEODSS sensors and ES-MCAT. Note that ES-MCAT fills a gap in current GEODSS GEO belt coverage.

2.1 JOHN AFRICANO OBSERVATORY

JAO was constructed on Ascension Island in 2014-15. Figure 2 shows the approximate location of JAO and ES-MCAT on Ascension Island. JAO consists of the Consolidated Instrumentation Facility (CIF) communication and control room, the weather tower, the James R. Benbrook telescope (JRBT) facility, and the ES-MCAT facility (see Figure 3). The CIF provides communication between NASA JSC and the rest of the JAO. JAO uses a dedicated weather instrumentation system that feeds into ES-MCAT's automated control software, allowing remote and autonomous observations to be conducted safely. JRBT is a 0.4 m telescope that can be used in the future to conduct observations complementary to ES-MCAT operations. Finally, the ES-MCAT is a 1.3-m telescope that conducted the GEO survey detailed in this document.

Figure 2. Map of Ascension Island. Blue pin is the approximate location of JAO and ES-MCAT. Map courtesy of Google Earth. Google map's data were provided by the following: Google, Data SIO, NOAA, U.S. Navy, NGA, GEBCO, and Airbus.

Figure 3. Image of Cottar Hill on Ascension Island showing the CIF (large central building), weather tower (left in yellow circle), James Benbrook facility (right, foreground steel tower in yellow circle), and ES-MCAT facility (right background building in yellow circle).

Due to the remote location of the observatory, the system was designed to be fully autonomous. The weather instruments collect measurements of weather conditions to determine if it is safe to open the dome and operate the telescope. If weather conditions exceed safe operating conditions during the course of the night, the dome automatically closes. Nightly program files are uploaded to the telescope control computer that define the telescope pointings for the night. To maintain the facility and perform regular repairs of hardware and instrumentation, on-site visits are performed approximately quarterly. NASA also maintains an agreement with the USSF for regular on-island contractor maintenance support between these quarterly visits.

2.2 EUGENE STANSBERY-METER CLASS AUTONOMOUS TELESCOPE

Figure 4. An image of ES-MCAT as seen from the open shutter outside the facility. The 1.3 m telescope is the central white structure inside the yellow double horseshoe mount. The double horseshoe mount allows for rapid transit of the telescope through zenith to allow for constant tracking of resident space objects along any trajectory.

ES-MCAT, shown in Figure 4, is a f/4 Ritchey-Chrétien telescope developed by DFM Engineering, Inc. The effective diameter of the primary mirror is 1.3 m. Unlike standard astronomical telescopes, design requirements for ES-MCAT and its dome included an ability to track objects moving rapidly (faster than sidereal) across the night sky for potentially observing LEO objects. For this requirement, the Observadome 7 m dome has a 90-inch shutter aperture and 2 azimuth motors, and ES-MCAT makes use of DFM's double-horseshoe equatorial mount that allows for rapid, constant tracking across zenith.

For imaging capabilities, the Spectral Instruments 1100S CCD is employed. This 4096 × 4096 15 μm pixel (0.6″/pixel) CCD allows for a field of view of 0.68° × 0.68°.

2.2.1 Optical System Throughput

Before initiating the first GEO survey, the optical throughput of the system was calculated (Cruz, Buckalew, et al. 2021). After identifying each component of the optical system, individual optical response data were obtained from the respective manufacturers, shown in Figure 5. These optical component responses include the CCD quantum efficiency (QE), the reflectance of the primary and secondary mirrors, and the transmittance of the field corrector and CCD window.

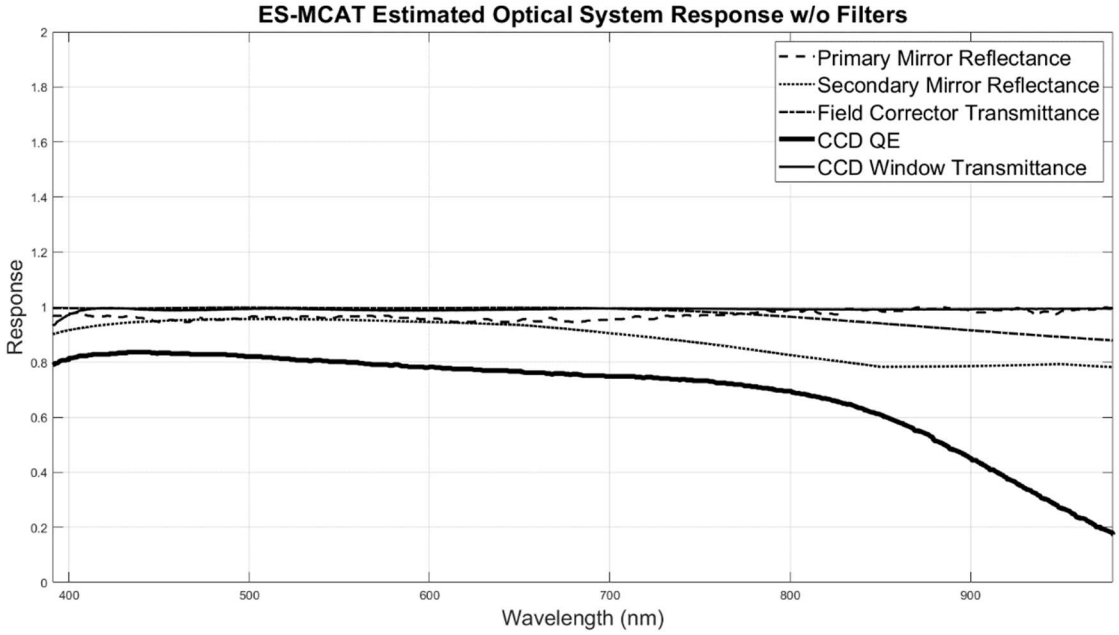

Figure 5. Optical system response between 390-980 nm for all optical components installed in ES-MCAT. Each contributes to the total throughput shown in Table 2.

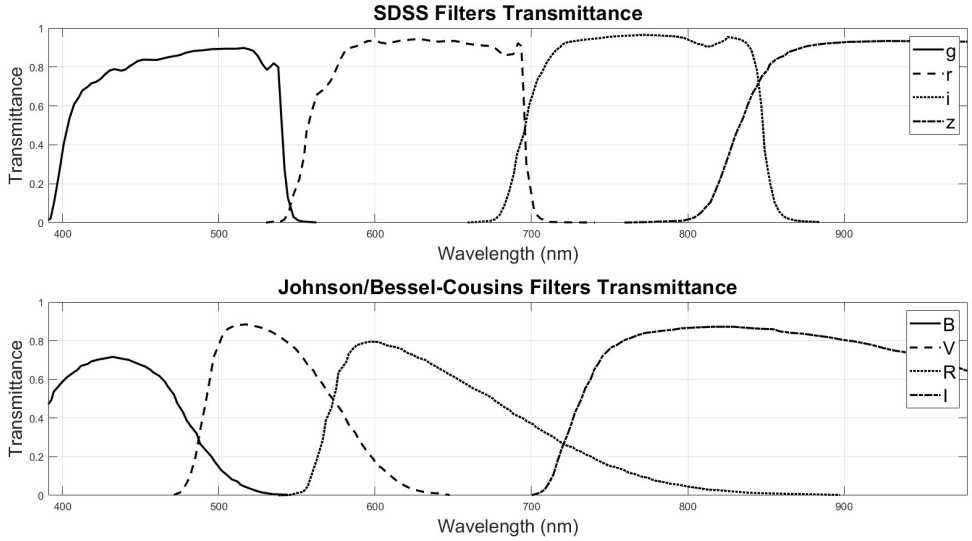

Figure 6. Transmittance of the SDSS g'r'i'z' and the Johnson/Bessel-Cousins BVRI filters. The filters labeled consecutively in the legends correspond to the filter curves from left to right.

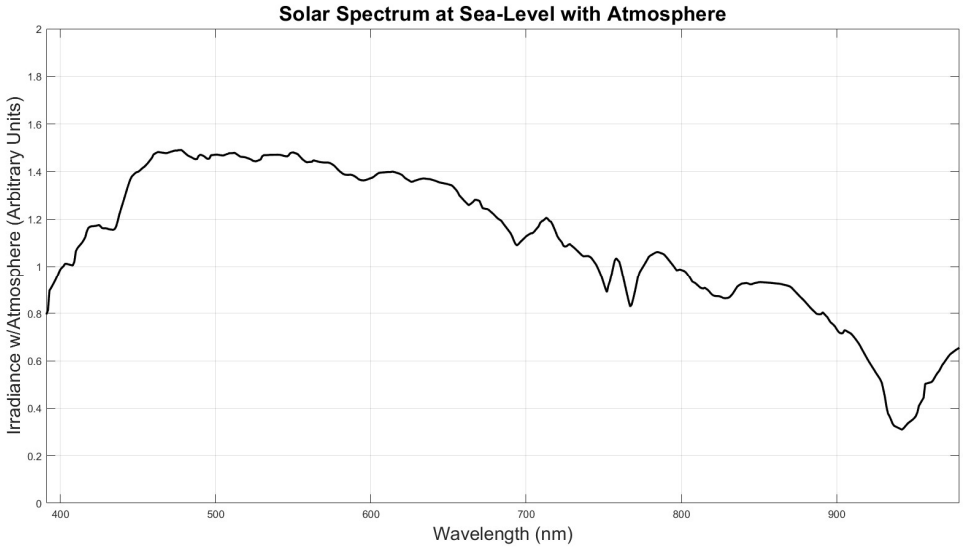

Figure 7. The average solar spectrum in irradiance or flux units, from 350-1000 nm at sea level (Newport Corporation 2021-2025).

The individual components' optical response data were linearly interpolated between the installed filter wavelength regions of interest, including the Sloan Digital Sky Survey (SDSS) g′r′i′z′ filters and the Johnson/Bessel-Cousins BVRI filters (see Figure 8). These reflectance curves were multiplied with the averaged solar spectrum at sea-level (see Figure 7). Finally, these products were integrated to give the total optical throughput in each installed filter bandpass for ES-MCAT. Figure 8 shows the full system throughput through the various filters, and Table 2 gives numerical values to the integration of the filter specific system throughputs. A more detailed explanation of the throughput calculations is found in (Cruz, Buckalew, et al. 2021).

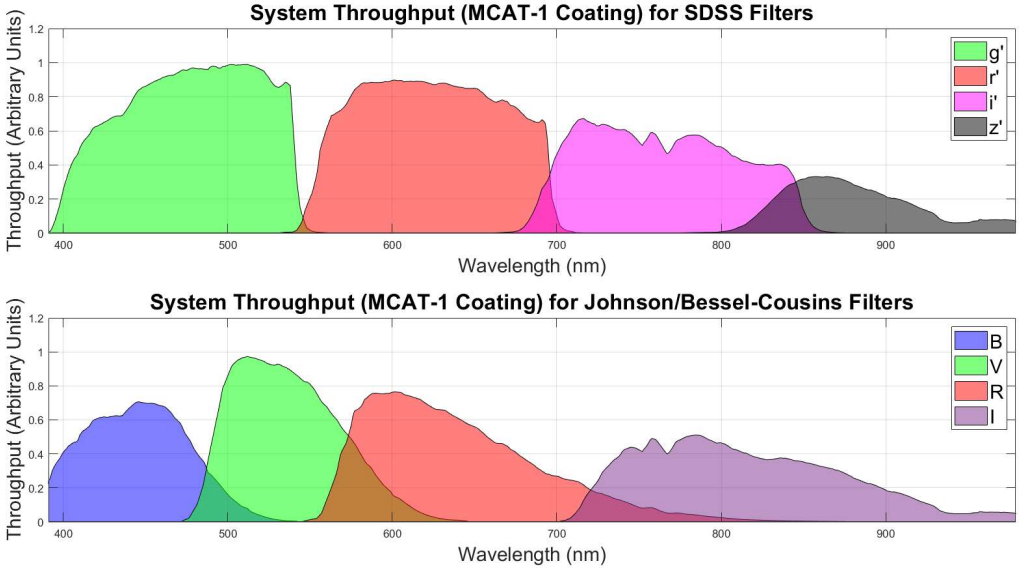

Figure 8. Full system throughput is shown for each filter bandpass. This includes all optical components and the effects of the solar spectrum (the typical source of reflected light from debris objects).

Table 2. Optical system throughput results for each optical filter that can be used with ES-MCAT (all optical components and atmospheric effects applied).

Filter	ES-MCAT 1 Flux (Arbitrary Units)
g′	118 ± 1.36
r′	116 ± 1.35
i′	82.8 ± 0.998
z′	30.9 ± 0.560
B	56.0 ± 1.04
V	81.6 ± 1.23
R	89.7 ± 1.22
I	75.5 ± 0.855

As shown in Table 2, the fluxes from the optical throughput analysis indicate that the SDSS g′ and r′ filters were ideal for observing resident space objects (RSOs) with ES-MCAT during the 2020-22 GEO survey. The flux values provided a basis for understanding the ideal optical characteristics of ES-MCAT and allowed for comparisons with changes to components.

2.3 CAPABILITIES OF ES-MCAT DURING THE 2020-22 SURVEY

2.3.2 Primary Mirror Reflectivity

The primary mirror was originally coated with a protected aluminum coating. In 2018, it was recoated with a protected, enhanced silver coating to provide increased reflectivity over what was achievable with aluminum (Lederer, et al. 2019). Over the years of the 2020-22 survey, the reflectivity percentage of the primary mirror evolved due to impacts from the COVID-19 pandemic.

The survey began in January 2020, which corresponded to the start of the COVID-19 pandemic and the soon-to-follow onset of global travel restrictions. The primary mirror was cleaned in February 2020 during a regular on-island maintenance trip. For NASA, international travel was banned soon thereafter until January 2021. Because of the travel ban, the telescope was operated, but the primary mirror could not be cleaned by trained personnel. At the time of the last primary mirror cleaning before the travel ban, the reflectivity was ~91%, acquired with a handheld scatterometer that uses a 670 nm laser. The reflectivity fell over the course of its operation in 2020, which was detailed with various measurements from the on-island USSF contractors. In January 2021, international travel resumed, allowing for trained personnel to travel to the facility and perform proper cleaning of the primary mirror. Unfortunately, this cleaning was too late into the mirror's degradation, and the primary mirror was stripped of its silver coating leaving only the nickel-chromium base metal. The cleaning did improve the reflectivity, but the best reflectivity of the nickel-chromium base (74%) is far below the 91% of the silver coating when cleaning consistently. With the silver coating gone, the nickel-chromium continued to degrade leading to its eventual demise with a final reflectivity of 57%. Figure 9 shows the evolution of the primary mirror's reflectivity over the survey period.

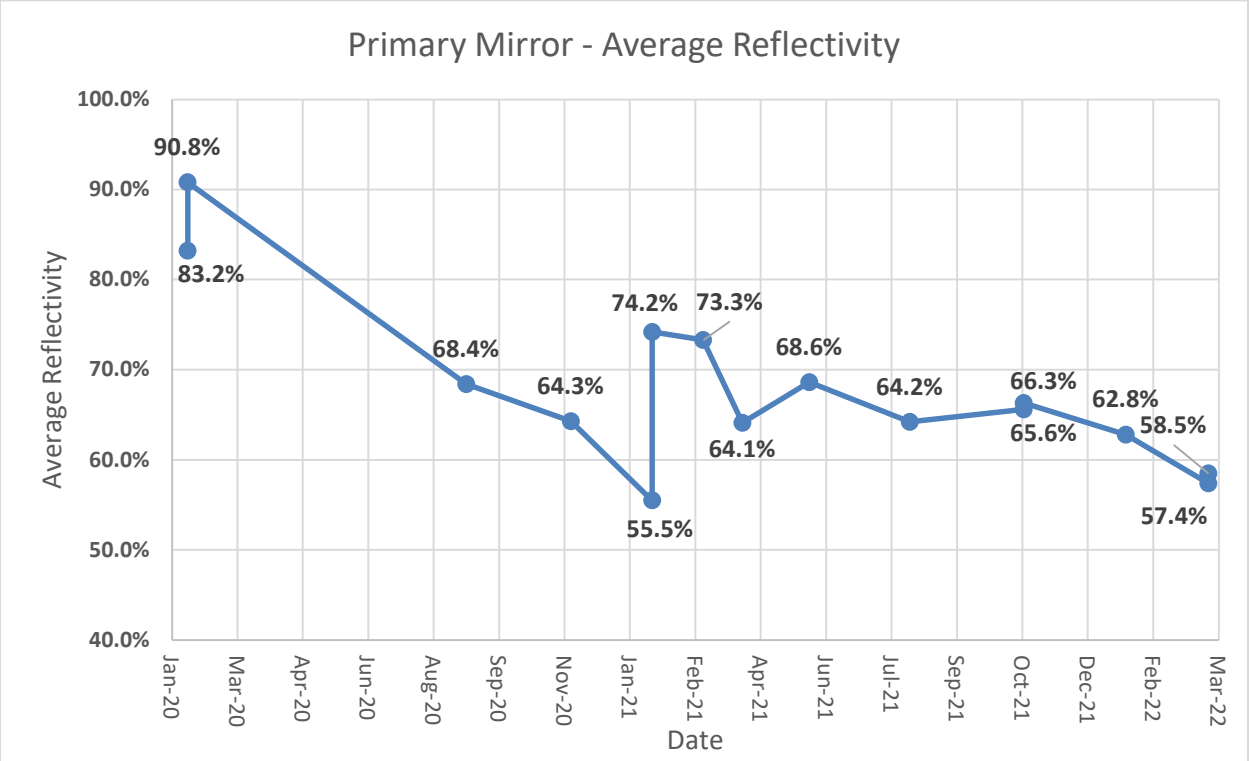

Figure 9. Average reflectivity of the primary mirror over the course of the GEO survey. The two vertical lines in January 2020 and January 2021 signify the average reflectivity before (lower value) and after (upper value) the primary mirror was cleaned.

Figure 10 shows the state of the primary mirror in December 2018, after reinstallation of the newly recoated mirror, and on 8 January 2021.

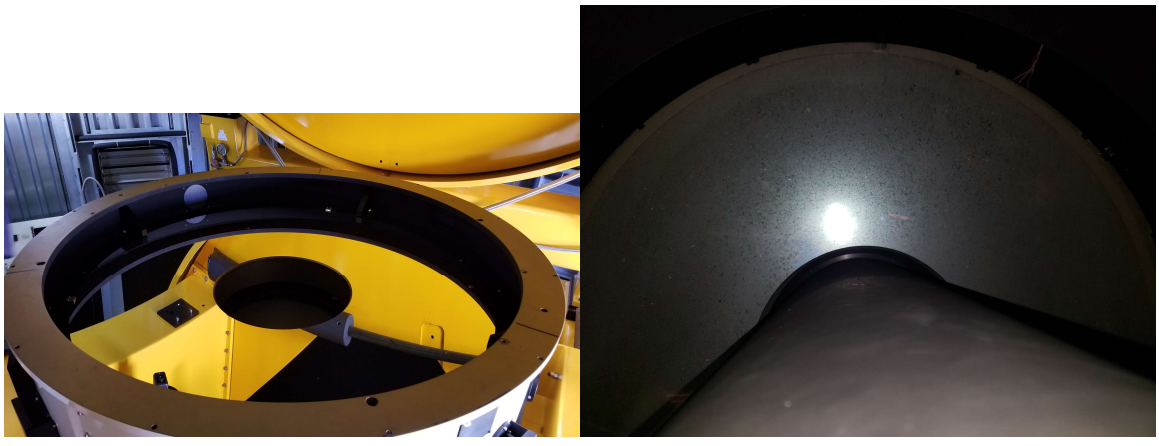

Figure 10. Left: The ES-MCAT primary mirror in December 2018. A clear reflection in the mirror is evident. Right: The primary mirror in January 2021 before cleaning. The oxidation had been occurring for 11 months. No reflection of the photographer is visible in this case.

2.3.3 *Limiting Magnitude*

In addition to the initial study of the optical system throughput, periodically analyzing the magnitudes from the dimmest detectable objects in a range of images and estimating a limiting magnitude from these values enabled continual checks of both the optics and software during the survey. Each night, standard star fields were acquired using the same filter(s) used for GEO survey images. The dimmest magnitudes from each sidereal-tracked (ST) image, found by Observatory Control System (OCS) using isophotal photometry with a minimum signal-to-noise ratio (SNR) of 6, are plotted in Figure 11 along with the measured primary mirror reflectivity.

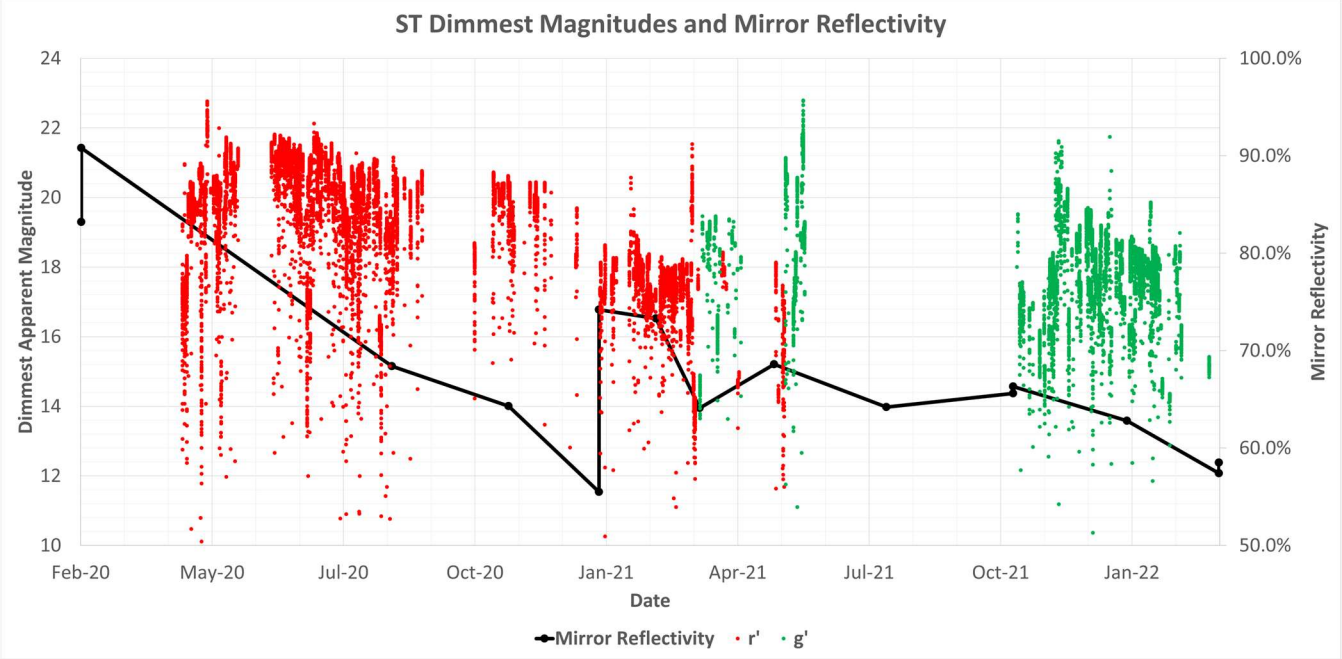

Figure 11. Dimmest magnitudes and mirror reflectivity values plotted over time. The dimmest g' and r' filter magnitudes for each image are represented by green and red dots, respectively, with the corresponding y-axis label on the left-hand side of the plot. Mirror reflectivity values are represented with a black dot and solid black line, with the corresponding y-axis label on the right-hand side of the plot.

The absence of dimmest magnitude datapoints between a range of dates in 2020 and 2021 was caused by unplanned maintenances. Periodic limiting magnitudes were estimated with these datapoints by selecting the most recent observational data spanning approximately two weeks and taking the median of the dimmest magnitudes over that time (Hickson 2019, Cruz, Buckalew and Arnold, et al. 2023). At the onset of the first GEO survey, with the use of an SDSS r′ filter and an exposure duration of 10 seconds, ES-MCAT's limiting magnitude was estimated as 19.48 ± 0.18. This magnitude represents objects approximately 10 cm in size when converted using the NASA OSEM (Barker, et al. 2004). These estimates were vital in monitoring the system and making adjustments remotely. For example, as the primary mirror coating degraded non-uniformly throughout the optical spectrum, a switch was made in early 2021 from using the SDSS r' filter to the SDSS g′ filter, which initially improved the limiting magnitude of the system by roughly one magnitude. Even with this change, the continued degradation of the primary mirror caused the limiting magnitude to drop to 16.63 ± 0.29, approximately 50 cm in size, at the end of the survey.

3.0 Data

3.1 SURVEY STRATEGY

The goal of the 2020-22 GEO survey was to achieve an expectation value (EVAL) of 0.3 or higher in a region of interest (ROI). The ROI is defined with RAAN and INC for all values of RAAN (0-360 degrees) and INC values from 0 to 20 degrees and covers a region in [INC*cos(RAAN), INC*sin(RAAN)] space centered at (7.5°, 0°) with a radius of 15°. This ROI was defined to best capture detections from GEO and near-GEO objects, which undergo precession under the influence of Earth's oblateness and the gravity of the sun and the moon. During this precession, an object's inclination will oscillate between 0° and 15° over a period of 50 years, and the angular momentum vector will trace a loop in [INC*cos(RAAN), INC*sin(RAAN)] space. Objects found to reside on or near this idealized loop represent GEO or near-GEO objects at various stages in their orbital evolution or objects perturbed by solar radiation pressure. Debris may originate or stray farther from this idealized path depending on the orbit and/or delta-velocity magnitude at the time of breakup. The EVAL is used to assign a detected object a weight, representing how many times that target should be counted when building populations for ORDEM. This weighting statistically accounts for multiple detections of the same object as well as detections of objects that are samples from a larger population that is, on average, undetected or under-sampled (Cruz, Buckalew, et al. 2021). The minimum value of 0.3 for the EVAL over this ROI was chosen based on previous experience with MODEST surveys.

A pointing strategy was developed for the first GEO survey to cover this ROI as uniformly as possible within the GEO debris belt over two years, while also allowing for certain lapses in coverage due to weather or facility downtime. Each night, a series of images were taken at two right ascensions (RA) and two declinations (Dec), with one set of RA and Dec during each half of the night. This was repeated for 24 more nights with decreasing Decs and increasing RAs, with the RAs trailing and leading the center of Earth's shadow by 15 degrees, and this 25-night pattern repeated for 350 nights. The resulting planned pointings are shown as green squares in Figure 12**Error! Reference source not found.**, descriptively named the "Candy-Cane Method." Note the size of the squares does not depict the size of the FOV for the telescope.

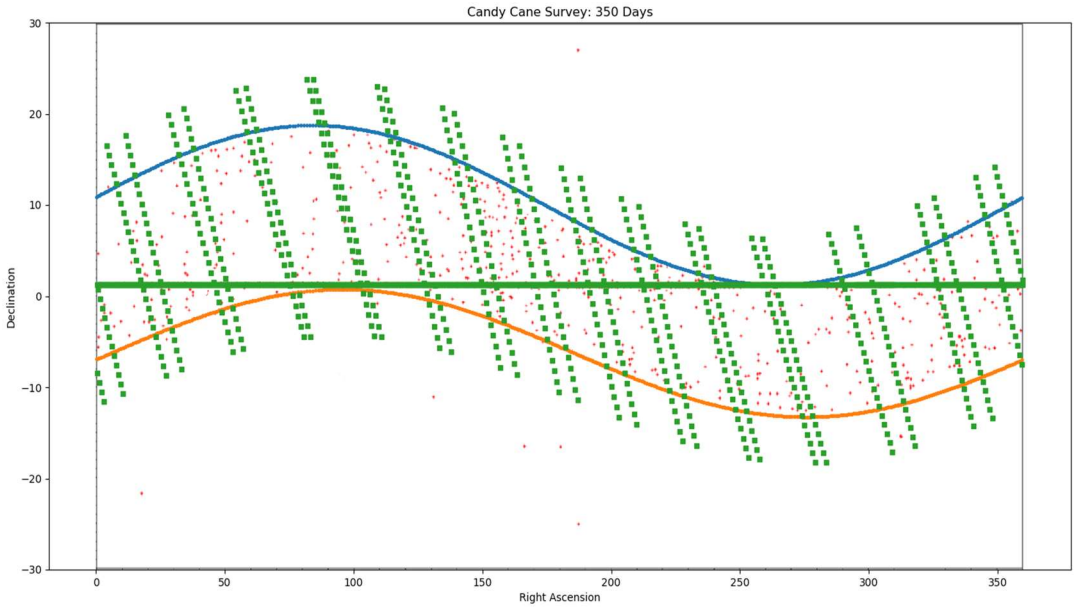

Figure 12. Daily motion of GEO objects (Dec versus RA) as seen from ES-MCAT. Red dots indicate cataloged (operational and inoperable) RSOs. The blue and orange lines bound the GEO belt of all known RSOs at GEO. The green squares represent planned field centers over 350 days (approximately the first year of the GEO survey).

Exposure times for all images were 10 seconds. The SDSS r′ filter was used for most images; however, the filter was changed to SDSS g′ when the mirror was degraded severely at the start of 2021 (see 2.3.3). Pointings were made such that the telescope was placed in one position with no motion in RA or Dec. For each pointing, a maximum of seven images were taken. Over this time, the Earth rotates causing the stars in the field of view to change position; thus, after the set of images was taken, the telescope was returned to the original RA and Dec position and the process was repeated.

To understand how this pointing strategy covers the ROI, the predicted field centers from the pointing strategy were processed through an in-house developed ODPO program, known as Tie-Dye, that simulates orbits with various INCs and RAANs based on the time of observation. This program was also used for previous telescopic measurements with MODEST (K. Abercromby, et al. 2008). The predicted coverage is produced with EVALs indicated by a range of colors. This program was run with the simulated effects from weather based on the average nightly availability on Ascension Island, which follows a cyclical pattern each calendar year as shown in Figure 13. On average, the nightly availability due to weather is approximately 40%.

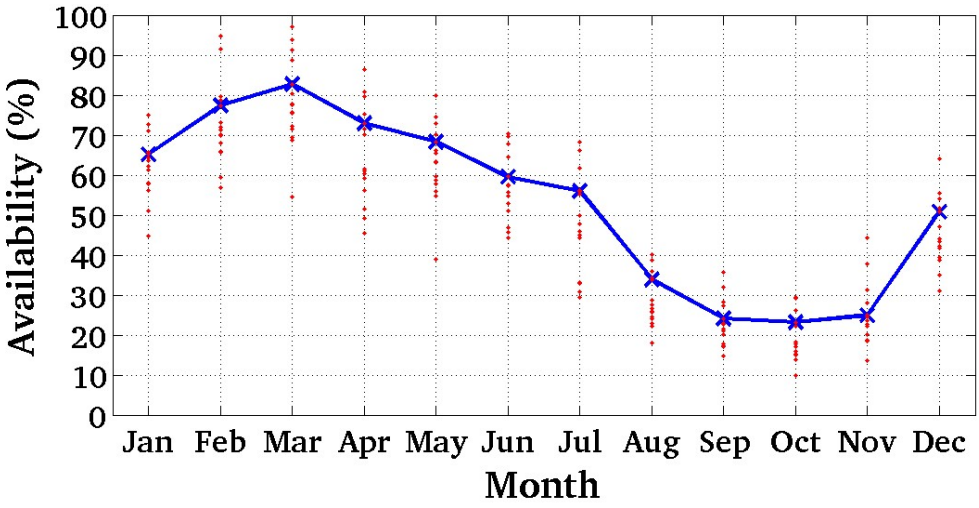

Figure 13. The estimated mean nightly availability of ES-MCAT on Ascension Island based on weather anomalies, binned per month. The observational availability is sinusoidal with a peak of 80% and a trough of 20%. Data courtesy of Randall Alliss, Northrop Grumman Corporation (Retired).

The effect of weather on the survey coverage is that certain regions of the Tie-Dye plot lose coverage, causing regions of the plot to show smaller total EVALs. The Tie-Dye plots are displayed in Figure 14 in both INC versus RAAN space and INC*sin(RAAN) versus INC*cos(RAAN) space. Even when incorporating the effects of average weather availability, EVALs across the ROI exceed the minimum goal of 0.3.

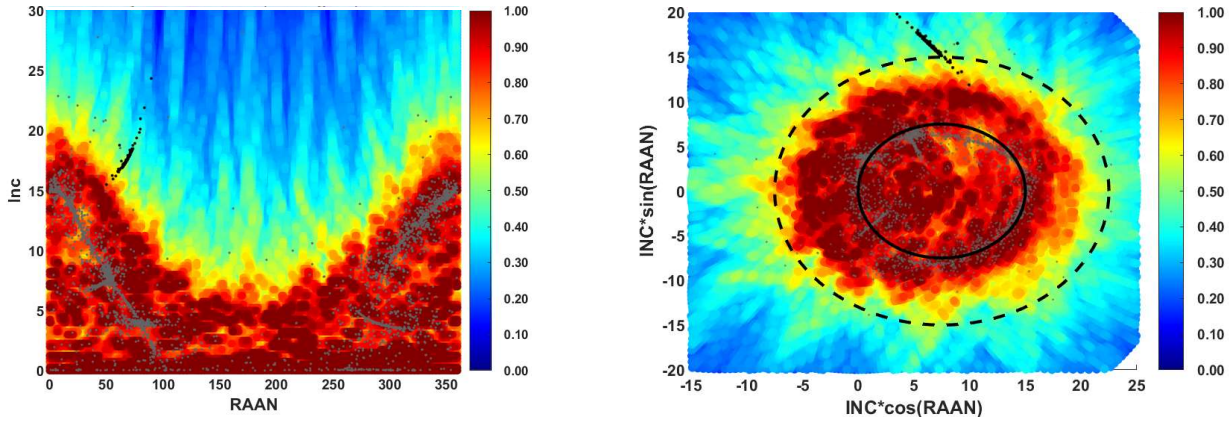

*Figure 14. Tie-Dye plots showing EVALs from 350 predicted field centers with a range of colors in INC versus RAAN space (left) and INC*sin(RAAN) versus INC*cos(RAAN) space (right). In both plots, modeled GEO objects (intact satellites and fragments propagated to late 2020) are shown with gray dots, and a modeled 2019 Titan Transtage breakup (propagated to late 2020) is shown with black dots. In the right plot, the outer dashed circle shows the region of interest, and the inner solid circle represents an approximation of the GEO belt. Note that the EVAL color bars are the same for both plots.*

3.2 DATA COLLECTION

Observations for the 2020-22 GEO survey started on 14 April 2020 and concluded on 12 April 2022. During these two years, GEO data were collected on 324 nights out of the possible 729 nights. A histogram of all nights is given in Figure 15 along with descriptive statistics of the histogram. Maintenance and weather resulted in the loss of 405 nights, 253 due to maintenance and 152 due to weather. The average night's observing hours of GEO data over all nights is 1.65

hours. When removing all nights lost due to weather and maintenance, the average hourly observation time increases to 2.47 hours. Because of weather impacts, data were never collected for the full 8 hours that were scheduled each night. The best night had 6.3 hours of observations. Additionally, the uptime for the telescope is presented in Figure 16. Each date's total hours spent on the GEO survey are presented as a bar, and the graph encompasses the entire two years. The large gaps are due to maintenance closures and not due to weather.

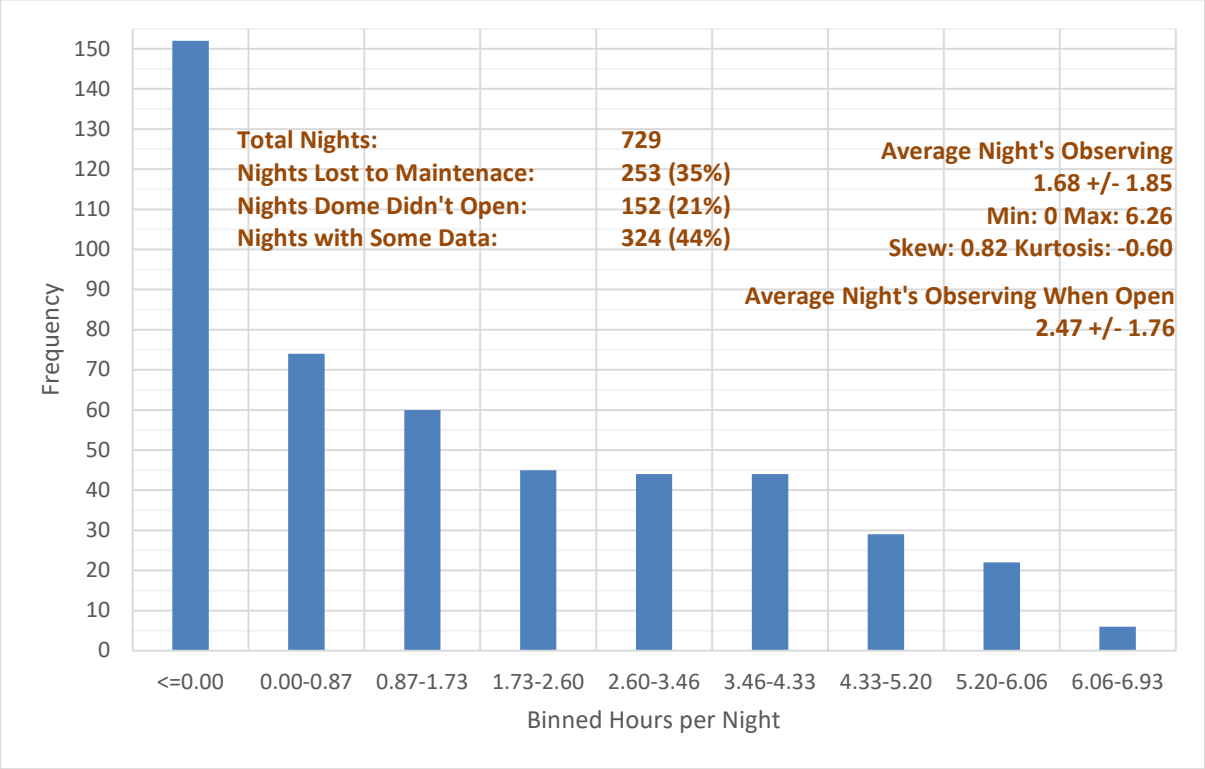

Figure 15. Histogram of all operational nights during the 2020-22 GEO survey, excluding nights affected by maintenance downtime. Bin titles are the number of GEO survey hours each night. Days in the <= 0.00 bin are those days where no data were collected due to weather. Descriptive statistics of the histogram are given at the top.

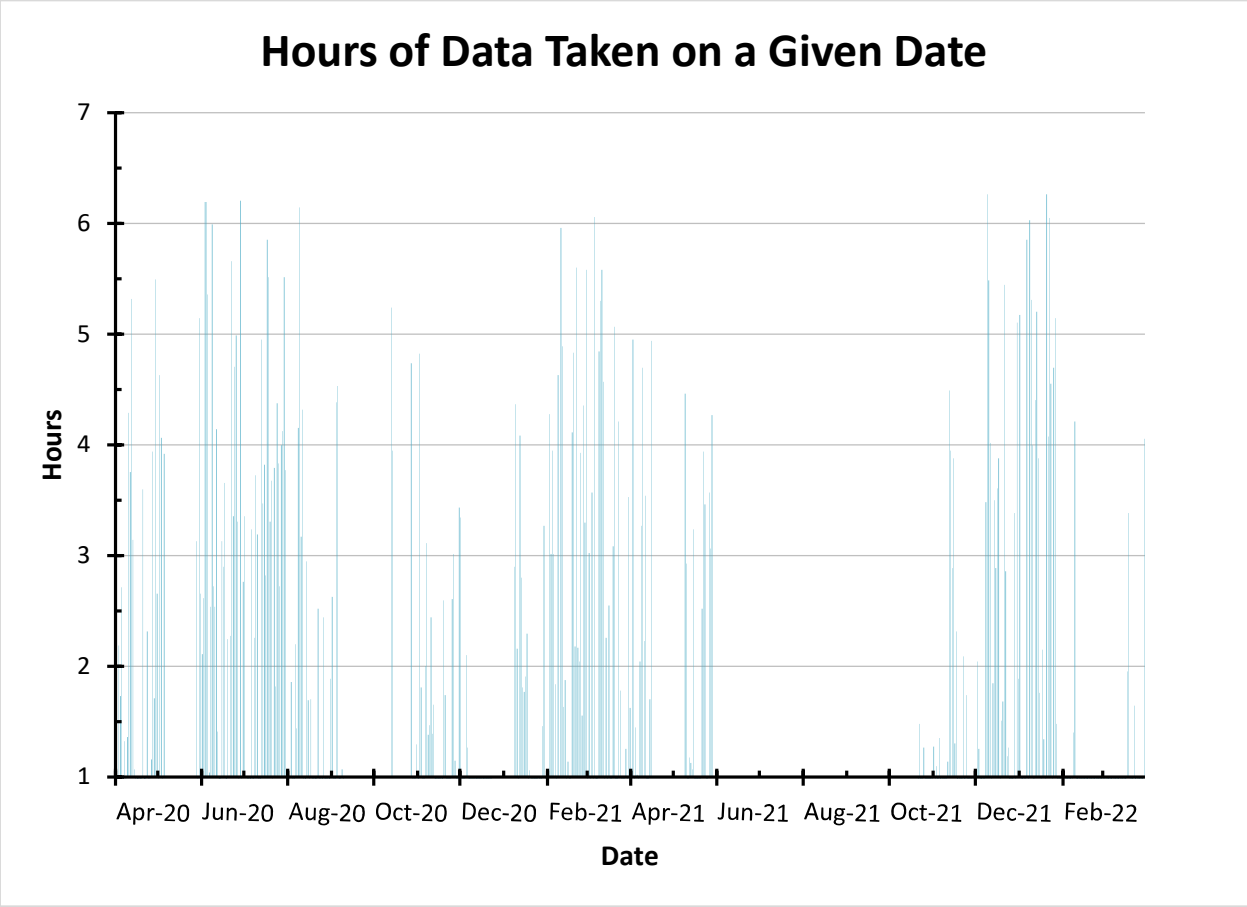

Figure 16. Bar graph of the hours of data taken on a given night during the GEO 2020-22 survey. Large gaps in observations are due to unplanned maintenances and not weather.

In addition to the effects of weather events like precipitation that cause the observatory to close, clouds often obscure the night sky so that objects cannot be successfully observed or calibrated. To reduce the amount of data collected that could not be successfully calibrated, data are only collected when the clouds are above a certain level of transparency. To measure this transparency, a forward-looking infrared (FLIR) camera is mounted at the end of the telescope that measures the infrared signature of the sky where the telescope is pointing. If the FLIR camera records a value greater than four (with possible values between zero and ten), the telescope waits to continue observations until the clouds clear and a lower FLIR value is recorded. Figure 17 shows the actual combined effects of weather and clouds on the hours of data taken on a given night during the survey.

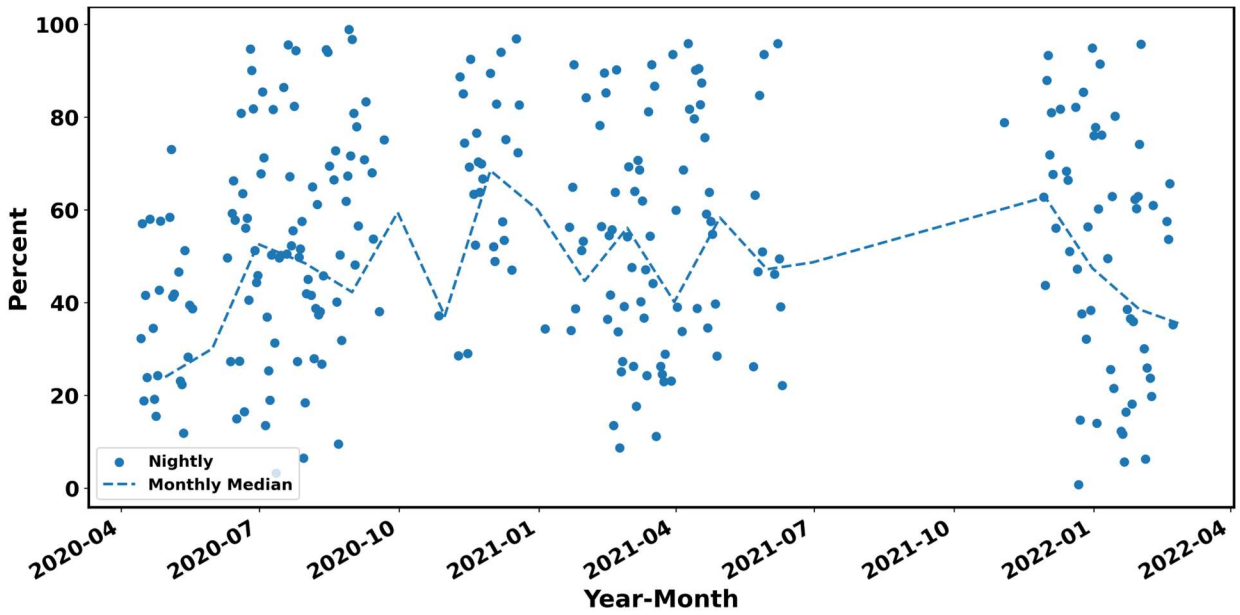

Figure 17. Percent of available hours lost to both weather events and clouds during the survey. Nightly hours lost and monthly medians are presented.

The observed field centers for the survey are shown in Figure 18. Field center differences between the planned pointings and the observed pointings are attributed to weather downtime, unplanned maintenance, and Moon brightness preventing useful observations. These effects also impacted the overall coverage in the ROI.

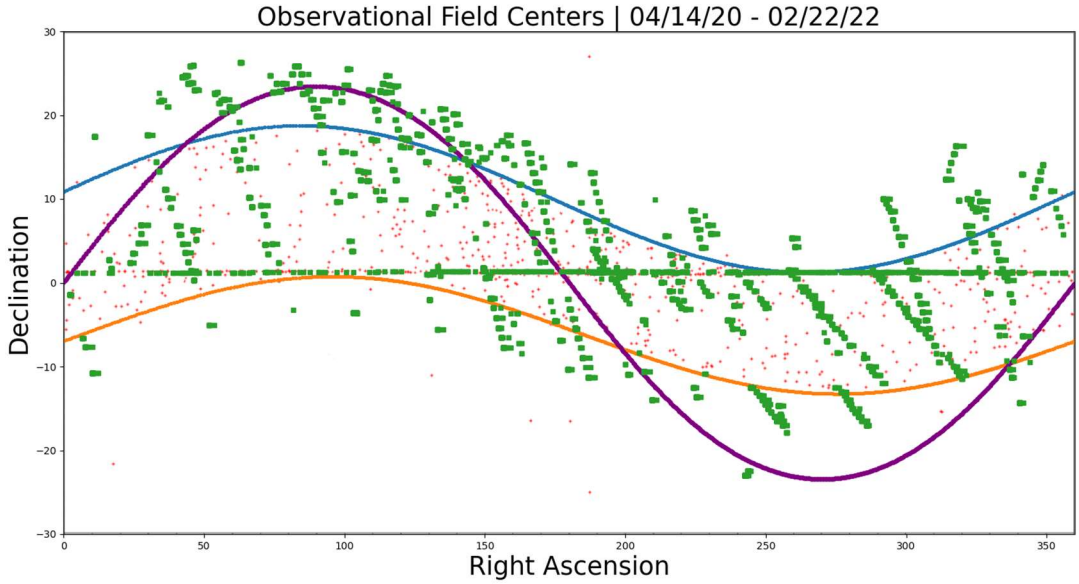

Figure 18. Observed field center pointings from the first GEO survey. Green squares represent observed field centers for each night, red markers represent cataloged GEO objects from January 2021, the blue and orange curve represent the approximate upper and lower bounds of the GEO belt, and the purple curve represents the path of Earth's shadow.

The Tie-Dye program used to estimate coverage in the ROI for planning the GEO survey was also used to calculate EVALs over the ROI for the observed pointings completed during the GEO survey. Field centers taken from each observation were processed and the resulting coverage and EVALs are found in Figure 19 in both INC versus RAAN space and INC*sin(RAAN) versus INC*cos(RAAN) space.

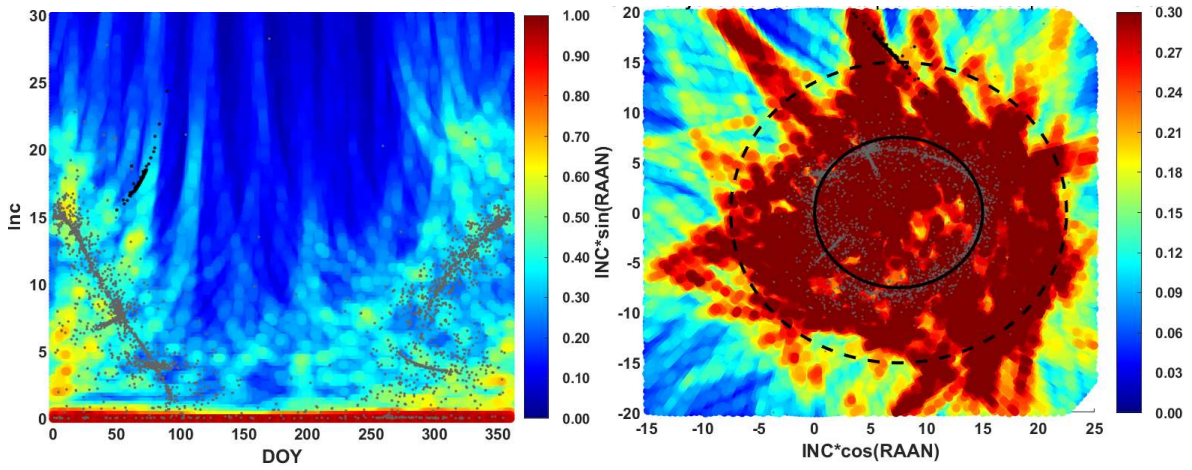

*Figure 19. Tie-Dye plots showing EVALs from observed field centers taken between 14 April 2020 and 22 February 2022 with a range of colors in INC versus RAAN space (left) and INC*sin(RAAN) versus INC*cos(RAAN) space (right). In both plots, modeled GEO objects (intact satellites and fragments propagated to late 2020) are shown with gray dots, and a modeled 2019 Titan Transtage breakup (propagated to late 2020) is shown with black dots. In the right plot, the outer dotted circle shows the ROI, and the inner solid circle represents an approximation of the GEO belt. Note that the color bars of both plots are not the same, with the right plot limited to a maximum of 0.3 corresponding to the EVAL goal for the GEO survey.*

In addition to these plots, the coverage in the ROI is calculated at different EVAL cutoffs and shown in Figure 20. The minimum EVAL of 0.3 was captured over 64.2% of the ROI. If the minimum EVAL is reduced to 0.25 or 0.2, the coverage increases to 84.2% or 93.8%, respectively, over the ROI. This provides additional information on planning for future surveys to ensure adequate statistical coverage of the ROI.

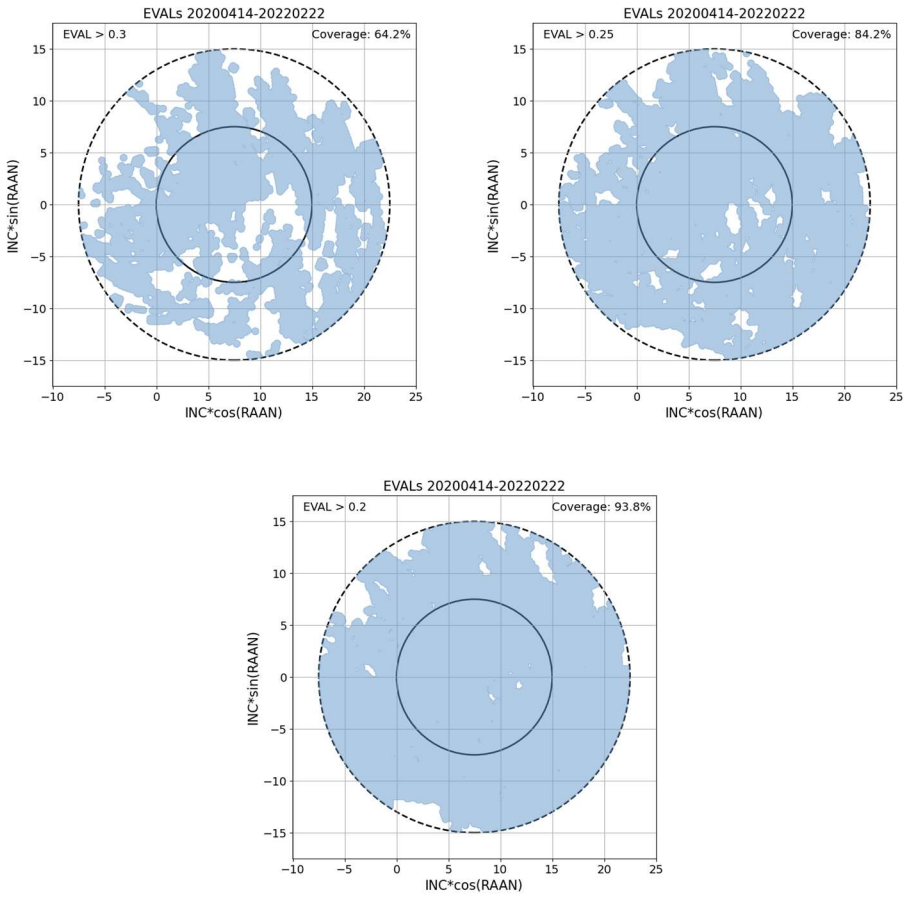

Figure 20. EVAL coverage plots from observed field centers showing field centers that have at least the minimum EVAL specified in each plot: 0.3 in the upper left, 0.25 in the upper right, and 0.2 in the lower graph. The ROI is specified with the outer dotted circle, and the percent coverage is shown in the top right corner of each plot.

3.3 DATA REDUCTION

Processing the GEO survey data uses the automated OCS software, developed by Euclid Software (Hickson 2019). Standard processing like bias subtraction, flat fielding, and cosmic ray removal are conducted. Astrometric and photometric calibration of the images utilize the GAIA DR3 (Vallenari 2023) survey results. An overview of the basic nightly observation and processing steps is shown in Figure 21.

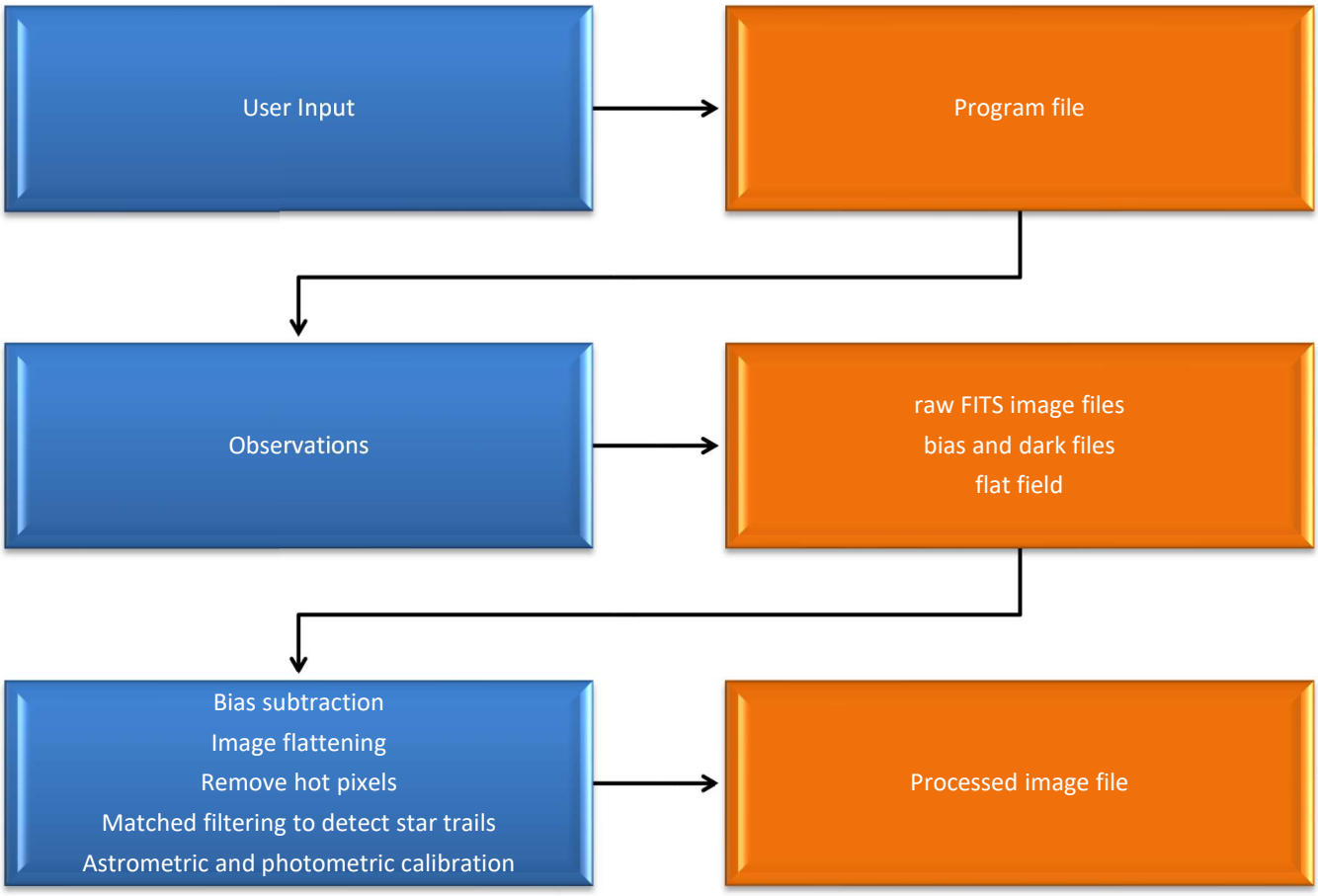

Figure 21. Overview of observations and basic processing with ES-MCAT.

Images collected during this survey were processed to identify object detections using both the automated OCS process as well as manual review. Manual review of the data was conducted because several instances were found of objects being missed by OCS. For manual review, two people independently review the data for each night that GEO images were taken, then any differences in object identification are reconciled. Review by two people minimizes potential human errors being introduced into the counting statistics.

3.3.1 Automated Object Detection

If an image is part of an image set of four or more images and the image is successfully calibrated, the image number and other vital parameters are recorded in a field center file (FCF). The FCF is used to assist with correlation (see Section 4.0).

Once OCS subtracts out the star trails, OCS calculates photometry on any potential objects (point sources or streaks) that are in the image. A configuration file provides the parameters for the aperture around these objects and the annulus for sky subtraction around the object. An initial minimum SNR threshold of 5.0 is used to identify valid detections.

Once photometry is completed for all images, the photometry objects identified in each image set of four or more images are compared with one another. Several restrictions are applied at this stage to filter out anomalous detections and objects not of interest for a GEO survey (*e.g.*, LEO objects). Without such restrictions, the false positive rate for detections would grow considerably. If the object found in all images in an image set has an angular rate in RA between 3.0″/s and 30.0″/s, then the object can be sent to the next threshold measure. Other restrictions are the Dec rate (between ±30″/s), minimum SNR (6.0), trail length maximum (150 pixels), minimum number of images (4), and maximum differences in the RA and Dec rate in all images in which the object was detected (0.06″/s for each). If an object meets all these restrictions, the object is called a target and passed onto the next stage of detection.

OCS saves all targets to a single, large, merged target file. Some of these targets are true objects while some may be a collection of cosmic rays and star trail detritus. Each target's position values are used to determine an orbit for the object. OCS calculates an initial circular orbit for each target and refines the orbit using the methods outlined in (Hickson 2019). A circular orbit assumption is necessary due to the short-time arc of observations. After all the refinements, and if the position uncertainty for the orbit is below the threshold value found in the configuration file (5.0″), the target is recorded as a true object in the object detect file. This file is used as described in Section 3.3.2 to determine if the object is correlated with any known RSO or is uncorrelated. A diagram summarizing the OCS object detection process and associated output files is shown in Figure 22.

In some cases, OCS may still identify some collections of star trails or hot pixels as objects in the object detect file. As a final data cleaning step, two people review reduced-size images of the detections listed in the object detect file to verify the objects are RSOs and not image artifacts. The final curated object detect file can then be used to derive further results as needed.

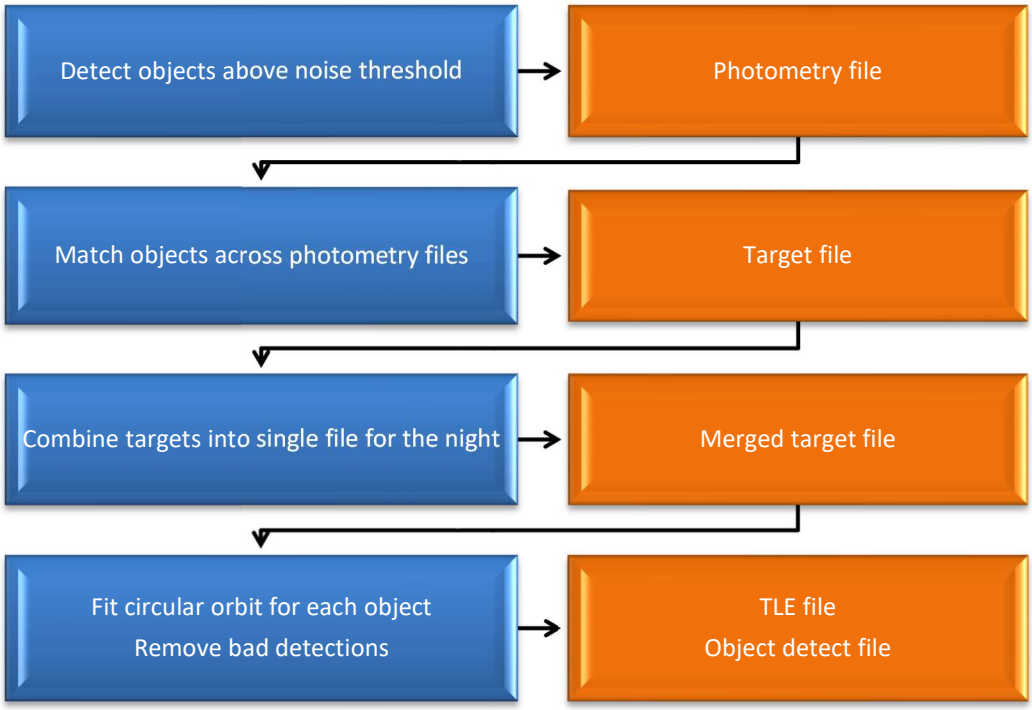

Figure 22. Overview of OCS object detection process.

3.3.2 Correlation of Targets using Correlation Software

OCS also correlates the detected objects with RSOs in the publicly available SSN catalog available at Space-Track.org. The *correlate* software uses the object detect file and FCF for a given night and compares the detected objects to two-line element sets (TLEs) for all cataloged RSOs. To minimize incorrect correlations, OCS uses 5 TLEs within ±30 days around the time of observation for each cataloged RSO. The TLEs are propagated from the TLE epoch to the time of observation using the Simplified General Perturbations 4 (SGP4) propagation method. If a detected object in the object detect file is matched to a cataloged RSO in one or more of the TLE files, the detection is assigned an SSN and categorized as a correlated target (CT). If the object is not correlated to a cataloged RSO, it is categorized as an uncorrelated target (UCT). UCTs dimmer than approximately 14th magnitude are likely to be debris objects and are of most interest for ORDEM purposes.

Once the correlation software is complete, two separate files are produced for the detected CT and UCT objects containing information about the objects' orbital parameters, SSNs (if they were correlated), dates/times of observation, and magnitudes. These parameters are important for inputting into the Tie-Dye program and ORDEM.

In addition to this information, the correlation software also produces a "NoSee" file, which lists the cataloged GEO objects that passed through the frame during the time of observation but were not correlated to a detected object. This file allows for diagnosis of the correlation software, ensuring that UCTs and CTs were correlated correctly, and determining the detection capabilities of the telescope and OCS/manual review. Finally, a "Human-In-The-Loop" file is created that includes "Miss Distances," defined as the differences in RA and Dec between a cataloged

object's estimated and detected positions and other outputs from the correlation algorithm. These Human-In-The-Loop files enable further diagnostics of the correlation software and OCS/manual review techniques.

4.0 Results

4.1 DETECTION RESULTS

While the survey was conducted until 12 April 2022, only data through 22 February 2022 was processed by OCS due to the degraded mirror performance. For this period, OCS detected 921 objects. Similarly, manual review was completed for data through 30 January 2021 due to time constraints in addition to degraded mirror performance and few objects detected after this date. Over this shorter time range, OCS detected 606 objects. Manual review was not limited to detections in a minimum of four images because humans are better able to discern differences of cosmic rays, star trails, and actual objects. Therefore, the threshold for the minimum number of images containing an object was set to two for manual review. With this criterion, manual review produced 1,078 objects from the data. Some objects detected by OCS were missed during manual review. Out of all the data reviewed, manual review failed to find 5 out of OCS's 606 detections, a failure rate of 0.8%.

A summary of the statistics of the detected objects for the OCS and manual review data is shown in Table 3. The numbers given for manual review here include detections from two or more images.

Table 3. Summary of detection statistics for OCS and manual review-processed data, including the date range of the processed data, total number of detected objects (CTs + UCTs), total number of CTs, and total number of UCTs. Manual review data includes all detections from two or more images, while OCS-processed data includes detections from the nominal four or more images.

	OCS-Processed Data	**Manual Review-Processed Data**
Date Range	14 Apr. 2020 – 22 Feb. 2022	14 Apr. 2020 – 30 Jan. 2021
Total Number of Detected Objects	921	1078
Number of Detected CTs	841	913
Number of Detected UCTs	80	165

4.1.1 Detection Magnitude Histogram Results

Figure 23 and Figure 24 display a comparison of the results of OCS to manual review between 14 April 2020 and 30 January 2021, but limiting the manual detections to those found in 4 or more images, consistent with the real object detection algorithm in OCS. With this criterion, OCS detected 606 objects compared to the manual review result of 745. Figure 23 shows the number of objects binned by apparent magnitude, and Figure 24 shows the corresponding percentage of objects found by OCS compared to manual review. Overall, OCS failed to detect 18% of the objects that manual review detected. Differences in detection rates of OCS and manual review are dependent on apparent magnitude and the RA and Dec rate restrictions used by OCS to reduce its results. Some of the differences between the magnitude distributions for OCS and manual review is attributable to differences in how the apparent magnitudes are calculated for each process. While OCS utilizes isophotal magnitude calibration with a minimum

SNR of 6.0, manual review magnitude calibration uses aperture photometry with no minimum SNR. This enables a magnitude calculation with manual review for objects that do not meet the minimum SNR threshold for OCS. Even with these differences in calculation, the OCS apparent magnitudes lie within the uncertainties of the manual review apparent magnitudes.

OCS detects greater than 80% of objects for magnitudes between 9 and 17. Manual review does outperform OCS for all apparent magnitudes. The failure of OCS at apparent magnitudes brighter than 9 mag is due to small number statistics and to these very bright objects being found in clusters along the GEO belt. OCS has difficulties with detecting point sources that are found close together. Thus, OCS missed 4 objects at these bright apparent magnitudes causing the value of 50% seen in Figure 24. The loss of objects beyond 18 mag is attributed entirely to OCS's criterion of the object having a SNR greater than 6.0 as well as the RA and Dec rate restrictions. These criteria were put in place due to OCS's propensity for interpreting cosmic rays as GEO objects.

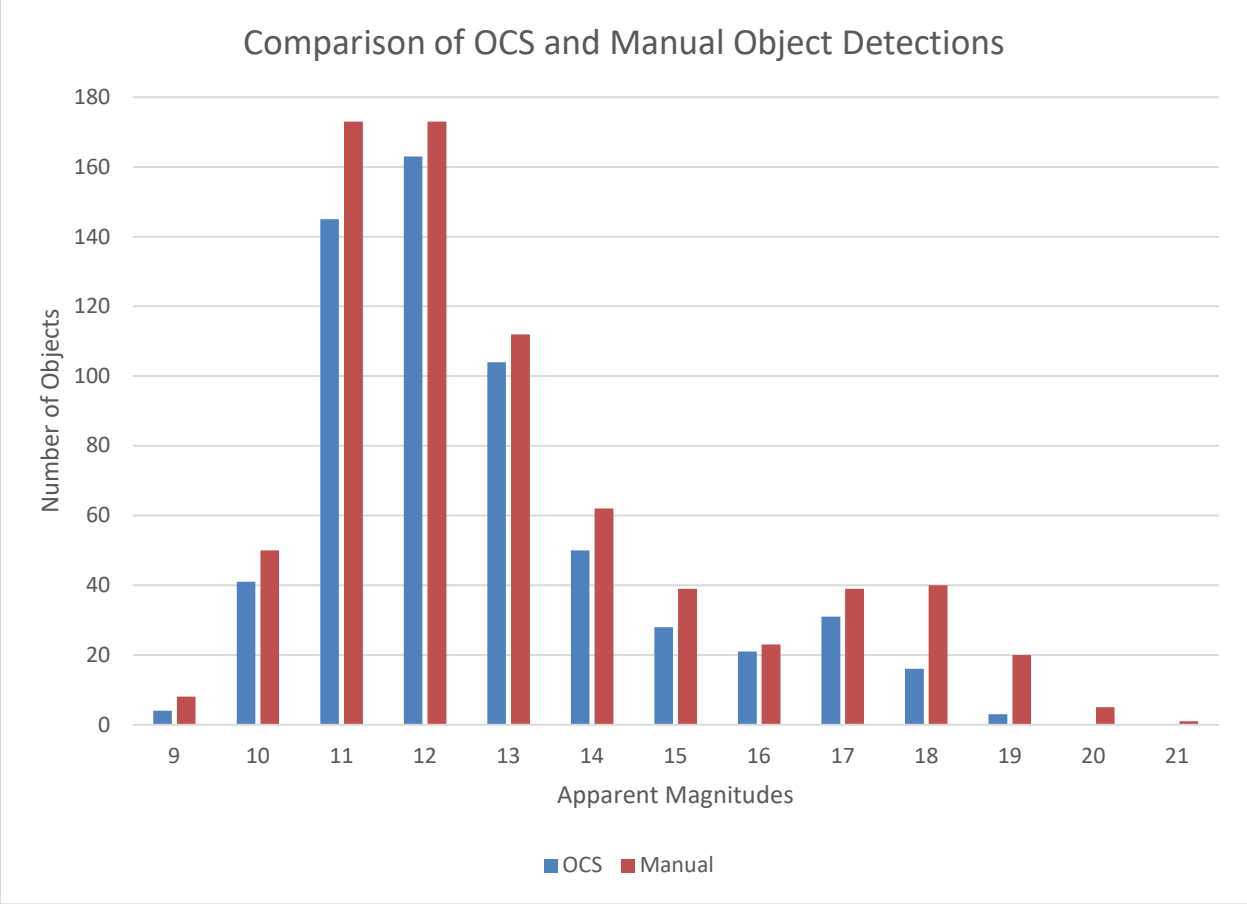

Figure 23. Histograms of the objects detected by OCS (blue) and Manual Review (red) between 14 April 2020 and 30 January 2021. Please note that labels for Excel histograms are right justified. Thus, 21 represents apparent magnitudes between 20 and 21.

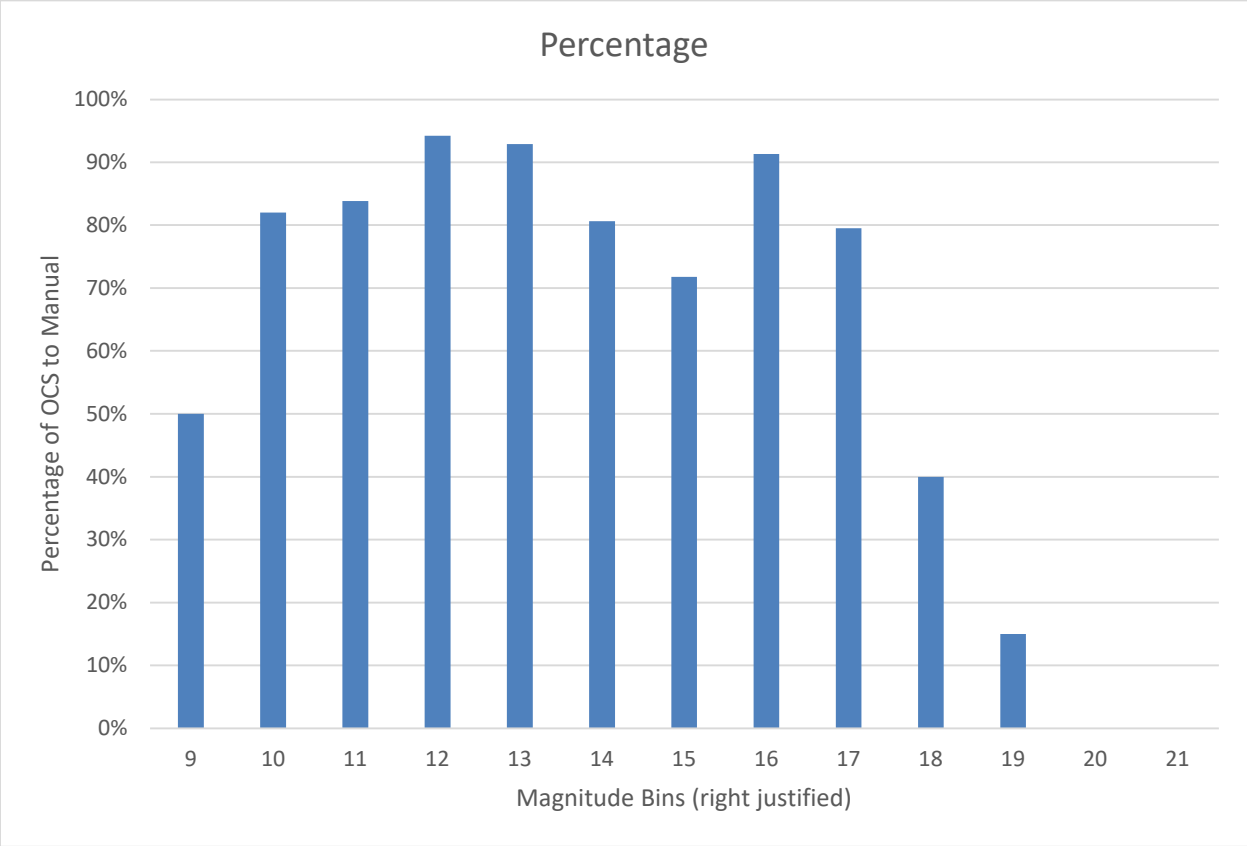

Figure 24. Histogram of the percentage of objects that OCS found relative to the manual review objects found between 14 April 2020 and 30 January 2021. Please note that labels for Excel histograms are right justified. Thus, 21 represents apparent magnitudes between 20 and 21. The 0% results in 20 and 21 reflect nonzero detections by manual review but 0 detections by OCS and thus are real and are not due to a lack of manual review data in these bins.

The detection results from both the OCS-processed data and the manual review-processed data can also be categorized by CTs and UCTs in an absolute magnitude histogram, which is presented in Figure 23. These absolute magnitudes were calculated from the median of the calibrated photometric apparent magnitudes of each image associated with a single detection to reduce aberrant magnitudes calculated with high cloud opacity, bad flat preprocessing, etc. Here, the results are shown for the full respective time frames: 14 April 2020 – 22 February 2022 for OCS and 14 April 2020 – 30 January 2021 for manual review. In addition, the OCS results are presented as all detections from the standard four or more images, while manual review results are from two or more images.

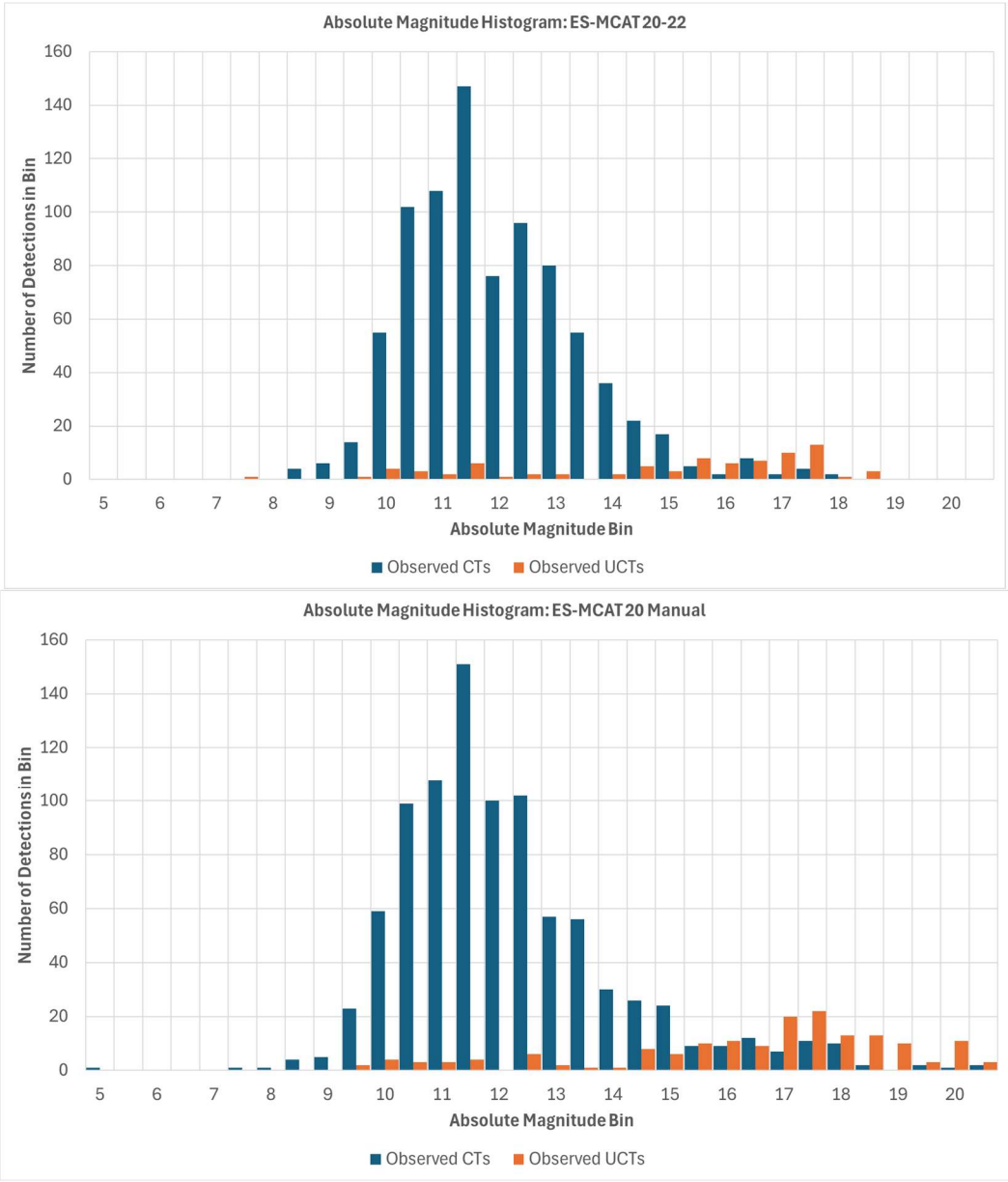

Figure 25. Absolute magnitude histogram of detection results from OCS (top) and manual review (bottom). Detections are separated by correlation results as CTs and UCTs. The peaks of the CT distributions for both processing methods are approximately 11.5 mag. The peak of the UCT distribution for both manual review and OCS-processed data is approximately 17.5 mag.

As noted above, manual review processing resulted in more CTs and UCTs as compared to OCS processing. There appear to be two distributions spanning the CT and UCT detections. The peak of these distributions appears to be similar for both processing methods when it comes to the CT and UCT detections at approximately 11.5 mag and 17.5 mag, respectively. Despite the OCS-processed data spanning a longer date range than the manual review data, manual review yielded more than double the number of UCTs. If a brightest magnitude cutoff of 14 mag is implemented for both OCS and manual review UCTs (recall UCT objects dimmer than this

magnitude are generally considered to be debris), OCS-processed data only has 57 objects in the ≥14 mag subset while the results from manual review were 139.

4.1.2 Detection Magnitude Evolution

To further understand the effects of the primary mirror degradation on fully processed data and detected objects, the detected objects' magnitudes were plotted for both processing methods over time. The effects of the primary mirror on the detection capabilities were estimated previously with limiting magnitude and completeness studies; however, the effect on the final data output of the GEO survey is also apparent in Figure 26 and Figure 27 for CTs and UCTs, respectively.

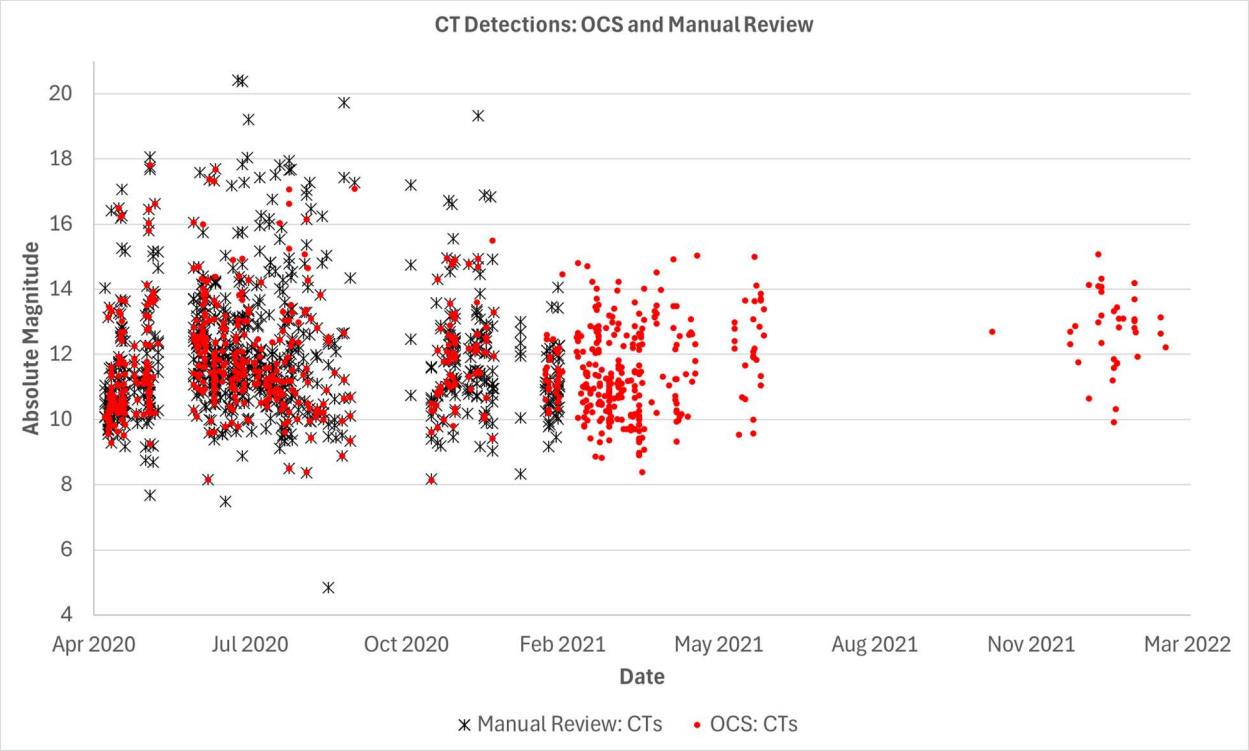

Figure 26. Scatterplot of CT detection absolute magnitudes over the duration of the GEO survey. Manual review data are represented by black X's while that of the OCS-processed data is represented by red dots. The manual review dataset spans through 30 January 2021 while the OCS dataset spans through 12 April 2022. Refer to Table 3 for more information.

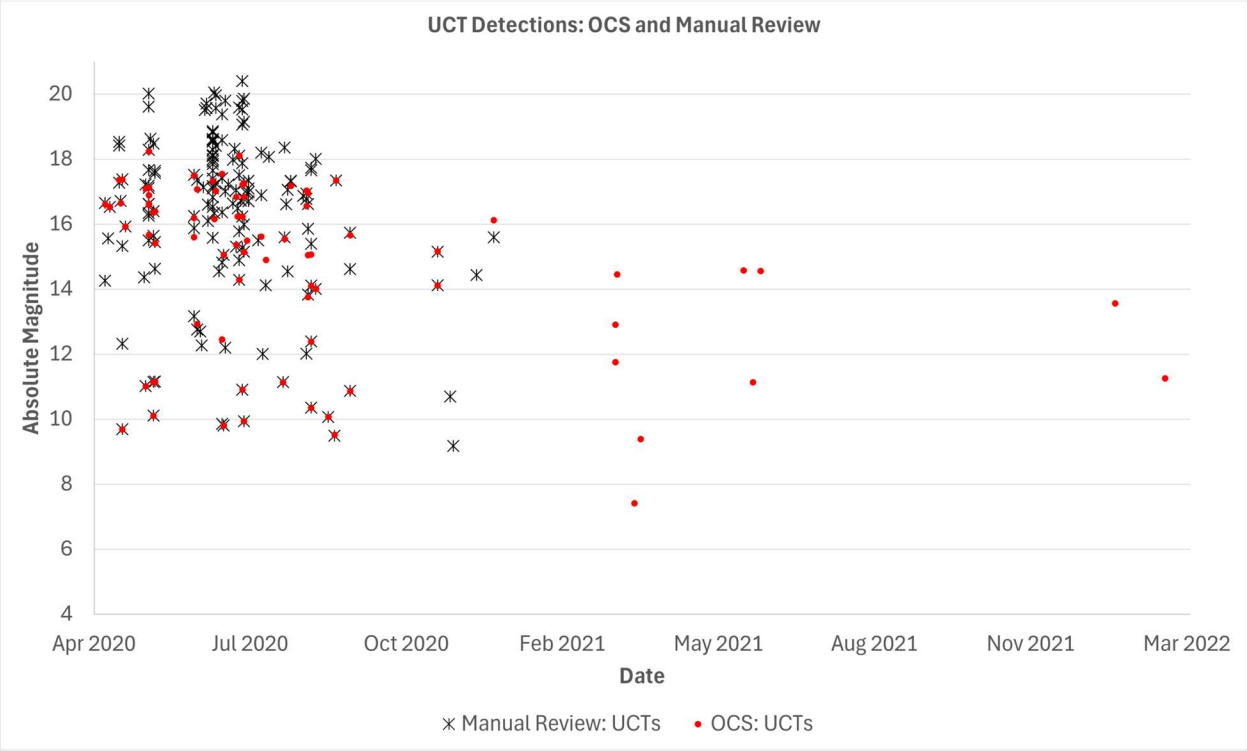

Figure 27. Scatterplot of UCT detection absolute magnitudes over the duration of the GEO survey. Manual review data are represented by black X's while that of the OCS-processed data are represented by red dots. The manual review dataset spans through 30 January 2021 while the OCS dataset spans through 12 April 2022. Refer to Table 3 for more information.

While the OCS-processed data spanned a longer length of time, in both cases of CT and UCT detections, manual review resulted in more dim objects in the final datasets. Still, manual review was affected by the mirror degradation as the dimmest detected objects become brighter over time in both figures. Despite this, manual review managed to detect dimmer objects than OCS even at the end of the dataset in January 2021 when the primary mirror was significantly degraded.

There are a significant number of overlaps between manual review and OCS detections. Some of these overlaps can be seen in the two figures above, while some appear to show slight differences in absolute magnitude. These differences are likely due to the different magnitude estimation techniques used in OCS versus manual review as discussed above. For a given object that exists in both the OCS and manual review datasets, if an image in the total image set was too cloudy for OCS's photometric calibration, then manual review software was used to calibrate that image. These magnitude differences tend to be within 3σ of their respective uncertainties.

4.1.3 Detection INC/RAAN Results

The POSORBs files created by the correlation software are inputs into the same Tie-Dye program used to produce predicted and actual observed coverages in the previous sections. With the POSORBs files, Tie-Dye now produces EVALs of actual detections. These detection positions and EVALs are visualized on plots in INC versus RAAN space at the times of observations for data processed through both OCS and manual review in Figure 28. They are

also presented on plots in INC*sin(RAAN) versus INC*cos(RAAN) space in Figure 29. Each colored point in the plots is a detected object, color-coded by its EVAL. Parent bodies of known GEO breakups are also shown, with elements extracted from their TLEs at a common epoch of 1 January 2021 for comparison with the detected objects.

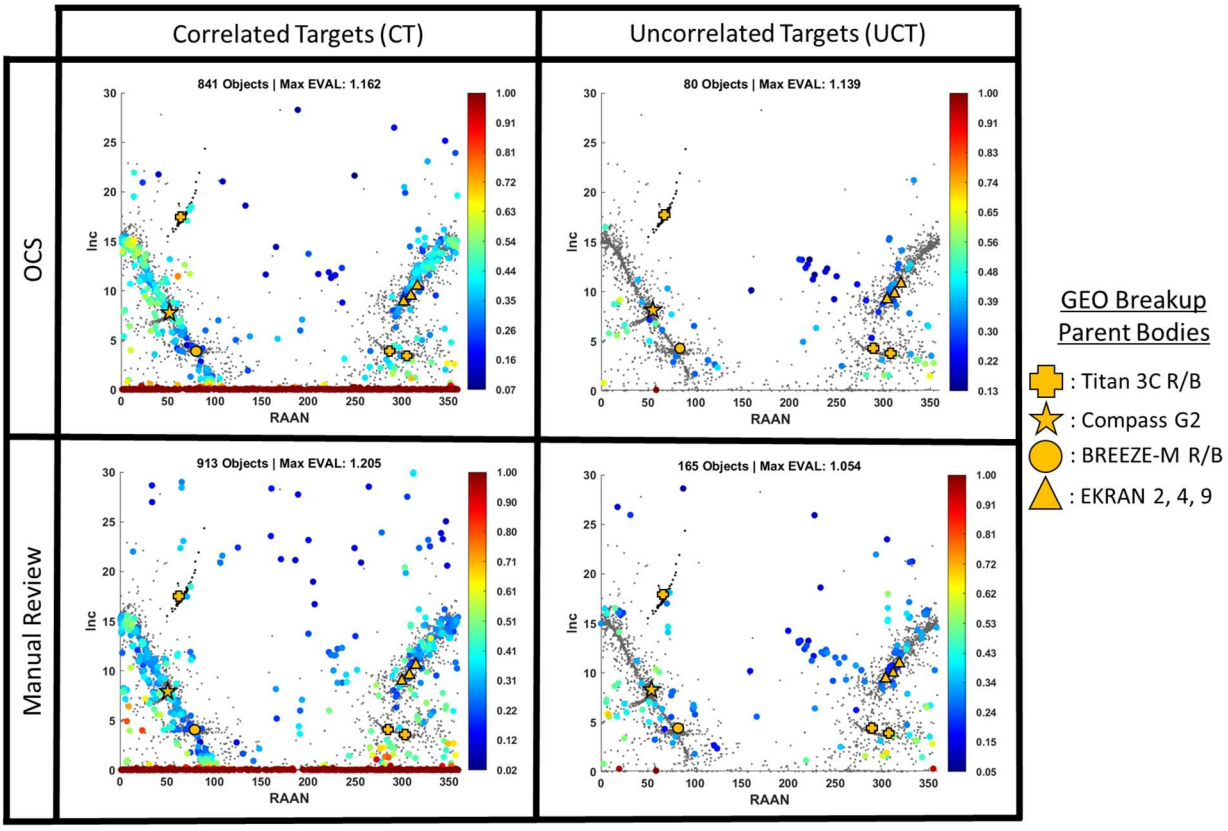

Figure 28. Tie-Dye detection plots from OCS and Manual Review processing of CTs and UCTs in [INC, RAAN] space. Modeled GEO objects (intact satellites and fragments propagated to late 2020) are shown with gray dots, and a modeled 2019 Titan Transtage breakup (propagated to late 2020) is shown with black dots. The EVALs within the plots are shown by a range of colors, indicated on the color bar on the right-hand side of each plot.

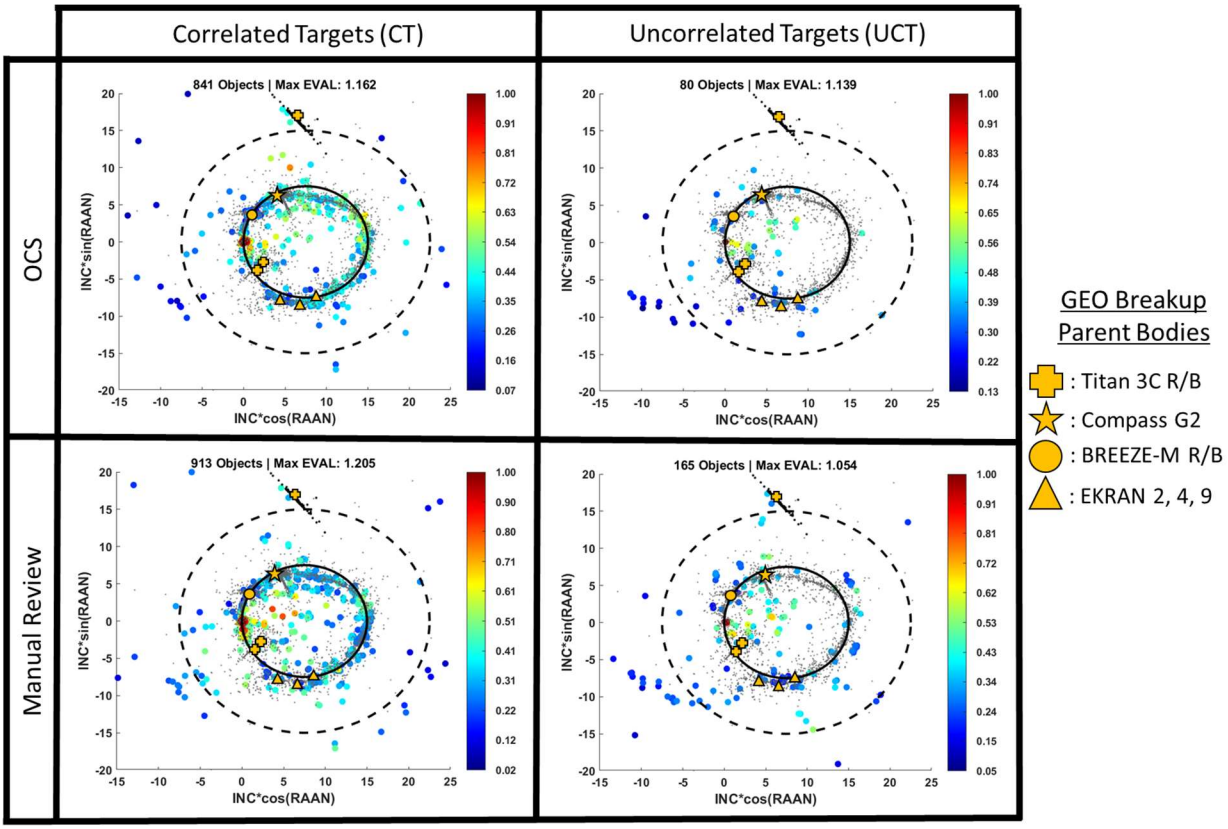

*Figure 29. Tie-Dye detection plots from OCS and Manual Review processing of CTs and UCTs in [INC*cos(RAAN), INC*sin(RAAN)] space. The dotted circle shows the ROI, and the solid line represents an approximation of the GEO belt. Modeled GEO objects (intact satellites and fragments propagated to late 2020) are shown with gray dots, and a modeled 2019 Titan Transtage breakup (propagated to late 2020) is shown with black dots. The EVALs within the plots are shown by a range of colors, indicated on the color bar on the right-hand side of each plot.*

4.1.4 Detection Orbital Characteristics

In addition to the Tie-Dye analyses performed on the detected objects, the OCS-processed and manual review data were characterized by their mean motions and inclinations to identify trends in the orbital families of the objects detected. Studying the objects' inclinations and mean motions roughly gives an indication of their orbit types: GEO, GTO, MEO, and MEO-transfer orbit (MTO). In the case of correlated objects, these were further differentiated by object type - including active spacecraft, rocket bodies, and debris - and their inclinations and mean motions were extracted from their TLEs at a common epoch of 1 January 2021. This was done to remove effects of the circular orbit assumption, which is inaccurate for objects with highly elliptical orbits. For UCTs, their inclinations and mean motions were propagated from the observation date to the common epoch with an assumed eccentricity of zero. While it is known this is inaccurate for true GTO and MTO objects, the short-time arc of observations precludes an accurate elliptical orbit assignment. The propagation time from time of observation to the common epoch of 1 January 2021 is short, less than one year for any object detected during the relevant date range for OCS or manual review. As a result, the propagated orbital elements for UCTs do not change significantly from the observed, assumed circular orbit elements. Their propagated and observed orbits are effectively equivalent, and the derived mean motion and inclination can give some indication of their true orbit types.

The objects detected during the 2020-22 GEO survey by OCS are presented in INC versus mean motion space at the common epoch of 1 January 2021, categorized by object type, in Figure 30. Those objects processed with manual review are presented in the same fashion in Figure 31. Date ranges of the 2 datasets are as presented in Table 3. Parent bodies and cataloged fragments of known GEO breakups are also included for comparison, with orbital elements extracted from their TLEs at the common epoch. The approximate orbital regimes are noted with their notional boundaries indicated with a color gradient. While most of the objects detected by OCS include GEO and some GTO objects due to the RA and Dec rate restrictions (see Section 3.3.1), manual review identified some objects determined to be in MEO, MTO and GTO/Molniya-type orbits as those rate restrictions do not apply. More UCTs with GTO characteristics were also identified with manual review.

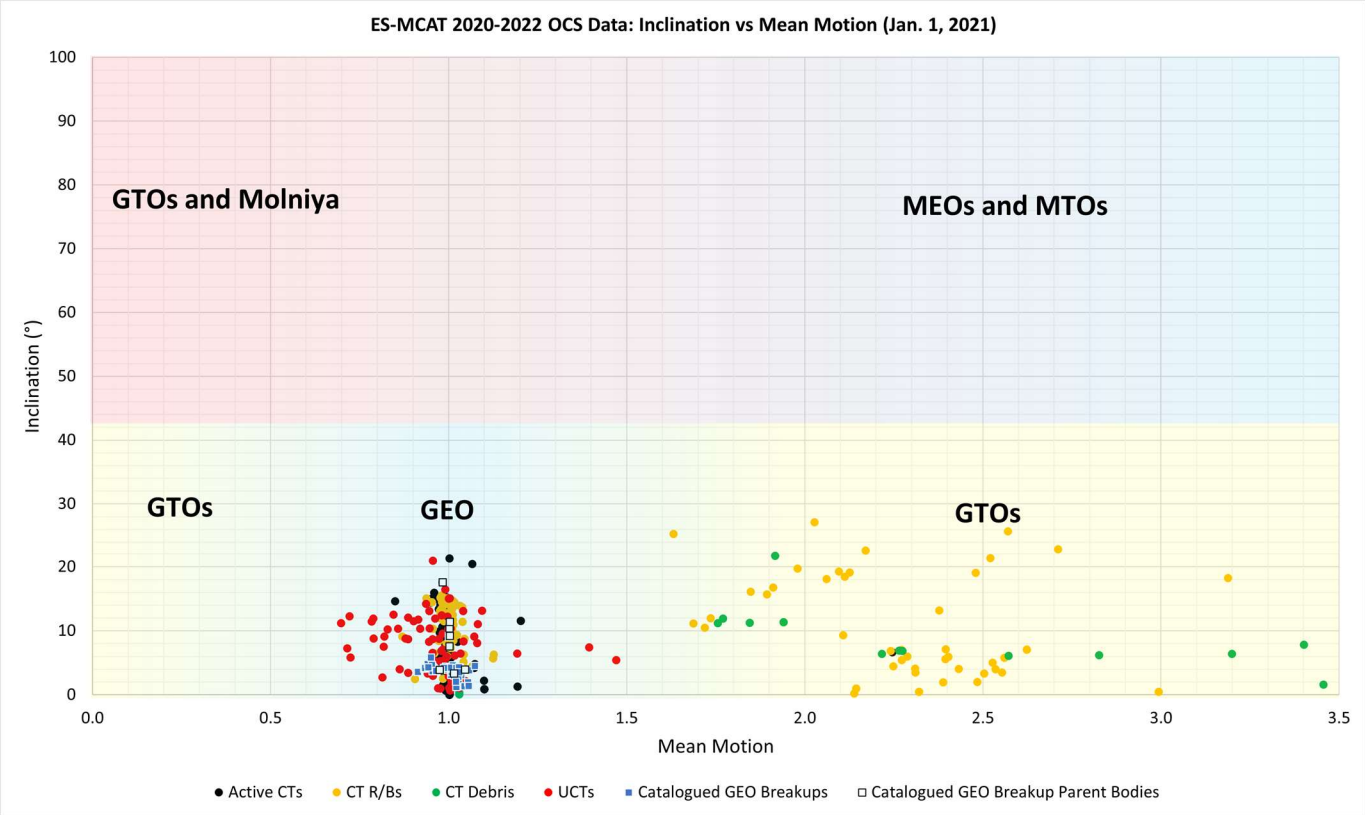

Figure 30. Orbital characterization plot of detected objects processed with OCS in INC versus mean motion space. Object types are noted in the legend at the bottom. Approximate orbital regimes are noted with their notional boundaries indicated by a color gradient.

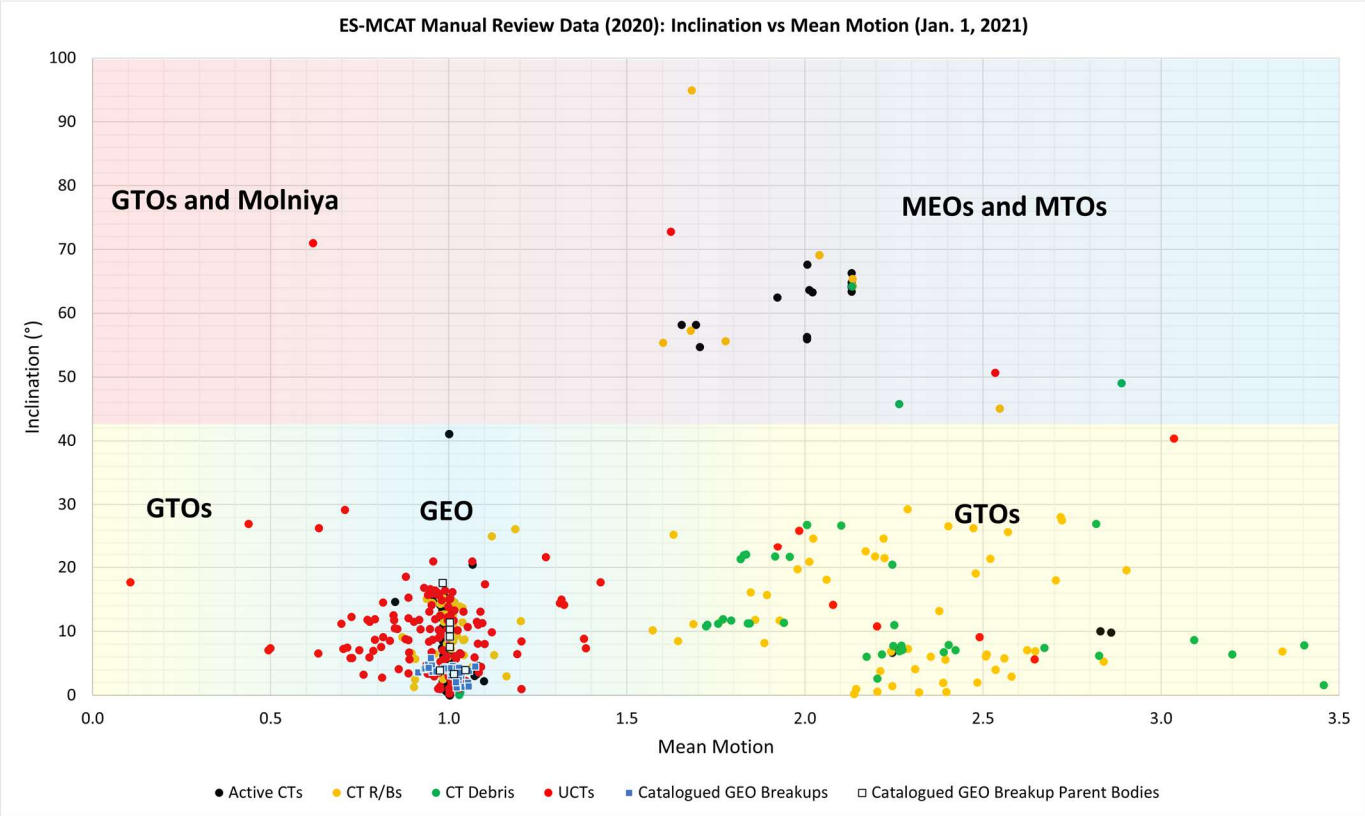

Figure 31. Orbital characterization plot of detected objects processed with manual review in INC versus mean motion space. Object types are noted in the legend at the bottom. Approximate orbital regimes are noted with their notional boundaries indicated by a color gradient.

5.0 Summary

This report provides details of the ES-MCAT observations, data, and the data reduction process of the GEO survey from 2020 to 2022 The survey lasted for 2 years, from 14 April 2020 through 12 April 2022. During that time, ES-MCAT observed for 2.5 hours on average per night for 324 nights out of the 729 possible. Data were processed using both the automated detection software OCS and manual review by two people. The OCS results over April 2020 to February 2022 included 921 objects, with 80 UCTs and 841 CTs. From April 2020 to January 2021, the data processed by manual review included 1078 objects, of which 165 are UCTs and 913 are CTs.

The absolute magnitude histograms in Figure 25 showed a peak for CTs at 11.5 mag for data processed with both methods. The absolute magnitude distribution for the UCTs is broad, covering the full range of measured magnitudes. Ignoring the brightest UCTs above 15 mag, the peak of the fainter distribution is 17.5 mag. Detections past 17.5 mag decrease down to the detection threshold of 21 mag. This faint end of the distribution reflects the detection capability of ES-MCAT and does not reflect the true nature of the GEO debris population. The true population is thought to continue through fainter magnitudes following the behavior of UCTs with brighter magnitudes (see Figure 25), as was shown when the statistical population was compared to the power-law distribution of breakups (K. J. Abercromby, P. Seitzer and H. M. Cowardin, et al. 2011).

6.0 Lessons Learned for Future Surveys

The planned survey positions presented challenges due to two choices made when starting coverage for the survey. The first was choosing positions that overlapped with the thin disk of the Milky Way galaxy. The background star trail density for these images in June and December made detecting RSOs impossible for OCS and difficult for manual review. The next survey will try and avoid the Galactic thin disk. For the 2023-25 survey, we have chosen an avoidance distance of ±5° about the Galactic plane (b=0° in Galactic coordinates). The second choice that limited object detections was the choice of distance to avoid the full moon. In the 2020-22 survey, the lunar distance avoidance was chosen to be 15°. Even with this hour radius avoidance zone, full Moon images were sometimes too saturated with sky emission due to the Moon. For the 2023-25 survey, we have increased the radius of the lunar avoidance zone to 30°. When the predicted field centers happen to occur inside of one of these overlaps, the RA or Dec are moved so that their locations are avoided. This leads to some field centers being exceptionally high or low in Dec.

In addition to improving the choices that made detections difficult, an attempt is being made to overcome the effects of weather to a limited extent. The weather on Ascension Island follows a roughly cyclical pattern (see Figure 13 and Figure 17). Based on this cyclical pattern, Dec values during the times of year that have lower estimated availability are spaced out in higher intervals. This enables the repeat of multiple pointings that are spaced out in shorter intervals in RA compared to those during the times of year that have higher nightly availability and increases the probability of detecting objects that may have been missed during observation time that was unavailable. Finally, while the 2020-2022 survey included nightly observations of the geostationary belt at 1.25° declination (as viewed from Ascension), the new survey strategy does

not include these pointings to reduce over-sampling of the geostationary region. This new survey method is illustrated in Figure 32.

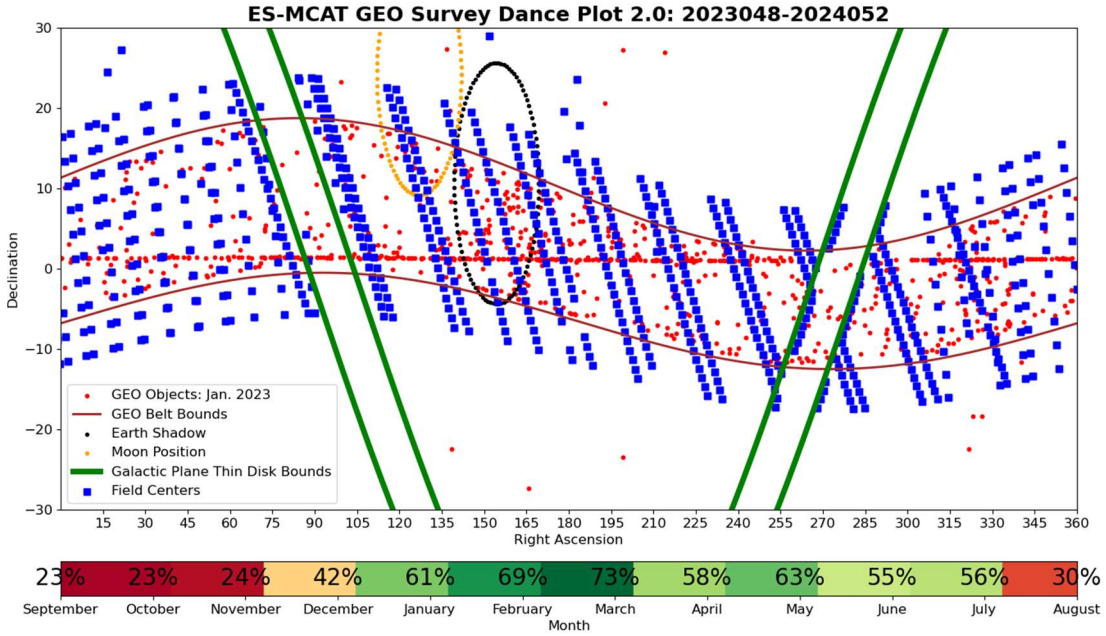

Figure 32. Planned field center pointings for a future GEO survey. Blue squares represent planned field centers for each night, red markers represent cataloged GEO objects from January 2021, and the brown curves represent the approximate upper and lower bounds of the GEO belt ±5°. The green curves represent the upper and lower bounds of the galactic plane thin disk. The orange dotted ellipse represents the moon's position ±15° (later increased to 30°), which moves based on its physical location in space. Finally, the black dotted ellipse represents Earth's shadow ±10°, which also moves in RA/Dec space. The bottom color bar represents the nightly availability (based on weather). The location of the month roughly coincides with Earth's shadow in RA at that time.

Another lesson learned was caused by the COVID-19 pandemic. Due to travel restrictions, the primary mirror could not be cleaned by trained personnel on the quarterly basis that kept the mirror in good condition in the years prior. Because of the lack of cleaning, saltwater spray accumulated on the mirror's surface and oxidized the silver coating. For ideal performance during future surveys, observations should not continue without cleaning the primary mirror at least every 3-4 months. If cleaning does not occur by then, observations should pause until cleaning can occur. From the data discussed here, a significant decrease in throughput performance was observed around six months post-cleaning. While observations should stop by six months without cleaning according to the data, oxidation occurs whether the mirror is exposed to salt spray or has already been exposed. By shutting the observatory after 3-4 months, the increased rate of salt spray accumulation is reduced, but the previous precipitates are still found on the surface.

7.0 References

Abercromby, K. J., P. Seitzer, E. S. Barker, H. M. Cowardin, and M. J. Matney. 2010. "Michigan Orbital DEbris Survey Telescope Observations of the Geosynchronous Orbital Debris Environment: Observing Years: 2004-2006." NASA/TP-2010-216129.

Abercromby, K. J., P. Seitzer, E. S. Barker, H. M. Cowardin, M. J. Matney, and T. L. Parr-Thumm. 2010. "Michigan Orbital DEbris Survey Telescope Observations of Geosynchronous Orbital Debris Environment: Observing Years: 2002-2003." NASA/TP-2010-216128.

Abercromby, K. J., P. Seitzer, H. M. Cowardin, E. S. Barker, and M. J. Matney. 2011. "Michigan Orbital Debris Survey Telescope Observations of the Geosynchronous Orbital Debris Environment: Observing Years: 2007-2009." NASA/TP-2011-217350.

Abercromby, K., P. Seitzer, E. Barker, H. Cowardin, and M. J. Matney. 2008. "A Summary of Five Years of Michigan Orbital DEbris Survey Telescope (MODEST) Data." *59th International Astronautical Congress, Space Debris Symposium (A6).* Glasgow, U.K.

Anz-Meador, P., J. Opiela, and J.-C. Liou. 2022. "History of On-orbit Satellite Fragmentations, 16th Edition." NASA/TP-20220019160.

Barker, E. S., K. Abercromby, H. Cowardin, and E. Stansbery. 2004. "Analysis of Working Assumptions in the Determination of Populations and Size Distributions of Orbital Debris from Optical Measurements." *Proceedings of the 2004 AMOS Technical Conference.* Wailea, Maui, HI. 225-235.

Cruz, C., B. Buckalew, J. Arnold, H. Cowardin, and A. Manis. 2023. "Updates of the Eugene Stansbery-Meter Class Autonomous Telescope for Geosynchronous Orbit Survey Operations." *Orbital Debris Quarterly News* 27 (1): 4-5.

Cruz, C., B. Buckalew, S. Lederer, and T. Kennedy. 2021. "Characterization of the Eugene Stansbery-Meter Class Autonomous Telescope for GEO Survey Operations." *Orbital Debris Quarterly News* 25 (1): 2-4.

Cruz, C., B. Buckalew, S. Lederer, K. Green-Tooney, P. Hickson, T. Kennedy, and H. Cowardin. 2021. "Characterization of the Eugene Stansbery-Meter Class Autonomous Telescope on Ascension Island." *Proceedings of the 2021 AMOS Technical Conference.* Wailea, Maui, HI. 390-401.

Hickson, P. 2019. "OCS: A Flexible Observatory Control System for Robotic Telescopes with Application to Detection and Characterization of Orbital Debris." *First International Orbital Debris Conference.* Sugar Land, TX.

Kennedy, T., M. Matney, H. Cowardin, A. Manis, A. Vavrin, J. Seago, D. Gates, P. Anz-Meador, and Y.-L. Xu. 2022. "NASA Orbital Debris Engineering Model (ORDEM) 3.1: Model Verification and Validation." NASA/TP-20220002309.

Lederer, S. M., B. Buckalew, P. Hickson, and H. M. Cowardin. 2019. "NASA's Orbital Debris Optical Program: ES-MCAT Updated and Upgraded." *Proceedings of the 2019 AMOS Technical Conference.* Wailea, Maui, HI.

Manis, A., M. Matney, A. Vavrin, J. Seago, D. Gates, P. Anz-Meador, T. Kennedy, H. Cowardin, and Y.-L. Xu. 2022. "NASA Orbital Debris Engineering Model (ORDEM) 3.1: Model Process." NASA/TP-20220004345.

Manis, A., M. Matney, P. Anz-Meador, and H. Cowardin. 2019. "The Updated GEO Population of ORDEM 3.1." *First International Orbital Debris Conference.* Sugar Land, TX.

Matney, M., A. Manis, P. Anz-Meador, D. Gates, J. Seago, A. Vavrin, and Y.-L. Xu. 2019. "The NASA Orbital Debris Engineering Model 3.1: Development, Verification, and Validation." *First International Orbital Debris Conference.* Sugar Land, TX.

Matney, M., P. Anz-Meador, A. King, A. Manis, J. Seago, and A. Vavrin. 2023. "An Overview of NASA's Newest Engineering Model, ORDEM 4.0." *Second International Orbital Debris Conference.* Sugar Land, TX.

Newport Corporation. 2021-2025. *Introduction to Solar Radiation.* Accessed 2021. https://www.newport.com/t/introduction-to-solar-radiation.

Stansbery, E. G., M. J. Matney, P. H. Krisko, P. D. Anz-Meador, M. F. Horstman, A. B. Vavrin, D. R. Jarkey, and Y.-L. Xu. 2015. "NASA Orbital Debris Engineering Model ORDEM 3.0 - Verification and Validation." NASA/TP-2015-218592.

Vallenari, A., et al. (Gaia Collaboration). 2023. "Gaia Data Release 3. Summary of the content and survey properties." *Astronomy & Astrophysics* 674: A1. doi:10.1051/0004-6361/202243940.